











Quantum spin liquid ground state in the trimer rhodate $\text{Ba}_4\text{NbRh}_3\text{O}_{12}$

Abhisek Bandyopadhyay ^{1,*}, S. Lee,² D. T. Adroja ^{1,3,†}, G. B. G. Stenning,¹ Adam Berlie,¹ M. R. Lees ⁴, R. A. Saha ⁵,
D. Takegami ⁶, A. Meléndez-Sans ⁶, G. Poelchen ⁶, M. Yoshimura ⁷, K. D. Tsuei,⁷ Z. Hu,⁶ Cheng-Wei Kao,⁷
Yu-Cheng Huang,⁷ Ting-Shan Chan ⁷ and Kwang-Yong Choi ⁸

¹ISIS Neutron and Muon Source, STFC, Rutherford Appleton Laboratory, Chilton, Didcot, Oxon OX11 0QX, United Kingdom

²Center for Artificial Low Dimensional Electronic Systems, Institute for Basic Science, Pohang 37673, Republic of Korea

³Highly Correlated Matter Research Group, Physics Department, University of Johannesburg, Auckland Park 2006, South Africa

⁴Department of Physics, University of Warwick, Coventry CV4 7AL, United Kingdom

⁵cMACS, Department of Microbial and Molecular Systems, KU Leuven, Celestijnenlaan 200F, Heverlee 3001, Belgium

⁶Max Planck Institute for Chemical Physics of Solids, Nöthnitzer Straße 40, 01187 Dresden, Germany

⁷National Synchrotron Radiation Research Center, 101 Hsin-Ann Road, Hsinchu 300092, Taiwan, Republic of China

⁸Department of Physics, Sungkyunkwan University, Suwon 16419, Republic of Korea



(Received 3 January 2024; revised 30 March 2024; accepted 2 April 2024; published 3 May 2024)

Frustrated magnets offer a plethora of exotic magnetic ground states, including quantum spin liquids (QSLs), in which enhanced quantum fluctuations prevent a long-range magnetic ordering of the strongly correlated spins down to lowest temperature. Here we have investigated the trimer based mixed valence hexagonal rhodate $\text{Ba}_4\text{NbRh}_3\text{O}_{12}$ using a combination of dc and ac magnetization, electrical resistivity, specific heat, and muon spin rotation/relaxation (μSR) measurements. Despite the substantial antiferromagnetic exchange interactions, as evident from the Weiss temperature ($\theta_w \sim -35$ to -45 K), among the Rh-local moments, neither long-range magnetic ordering nor spin freezing is observed down to at least 50 mK, in ac-susceptibility, specific heat, and zero-field μSR measurements (down to 0.26 K). We ascribe the absence of any magnetic transition to enhanced quantum fluctuations as a result of geometrical frustration arising out of the edge-sharing equilateral Rh-triangular network in the structure. Our longitudinal-field μSR result evidences persistent spin fluctuations down to 0.26 K, thus stabilizing a dynamic QSL ground state in $\text{Ba}_4\text{NbRh}_3\text{O}_{12}$. Furthermore, the magnetic specific heat data at low T reveal a significant T -linear contribution plus a quadratic T dependence, which may indicate the gapless Dirac QSL phenomenology of the spinon excitations with a linear dispersion.

DOI: [10.1103/PhysRevB.109.184403](https://doi.org/10.1103/PhysRevB.109.184403)

I. INTRODUCTION

A quantum spin liquid (QSL) is a novel magnetic state of matter without magnetic long-range order even at zero temperature due to strong quantum fluctuations. The ground state of a QSL does not invoke order parameters, and also there is no breakdown of the paradigm of Landau's symmetry breaking in this exotic state [1]. Investigations of materials hosting QSL ground states are of immense importance in the context of understanding the mechanism of high-temperature superconductivity [2,3], as well as for possible applications in data storage, memory devices, and future generation quantum computation [1,4–6]. Magnetic frustration can disrupt conventional long-range magnetic order and establish a quantum entangled ground state with nonlocal excitations [4,5,7–9]. Since Anderson's proposal of the “resonating valence bond”

in the antiferromagnetically interacting spin-1/2 triangular lattices [10], the search for QSLs in geometrically frustrated magnetic lattices has been one of the most fascinating quantum materials research topics. The spin-orbit entanglement of correlated electrons in $4d$ -Ru, Rh and $5d$ -Re, Os and Ir based oxides has opened up a promising new avenue in the exploration of a wide variety of quantum phenomena ranging from Kitaev QSLs to topological superconductors [11–15].

In particular, the heavier $4d$ and $5d$ transition metal based hexagonal perovskite oxides with face-sharing octahedral units and edge-sharing triangular network can accommodate a rich spectrum of frustrated quantum magnetism arising out of the unique combination of spin-orbital coupling (SOC), noncubic crystal distortion, hopping, covalent interaction, geometrical frustration, enhanced quantum fluctuations, and multiple magnetic superexchange interaction pathways [16]. Surprisingly, while the dimer-based $6H$ -hexagonal triple perovskites with a general formula $\text{Ba}_3\text{MM}'_2\text{O}_9$ (M = mono, di, tri, and tetravalent nonmagnetic cation; M' , any $4d/5d$ transition metal) have been extensively investigated from the viewpoint of quantum magnetism [7,17–25], to date, the trimer-based $12L$ -hexagonal quadrupole perovskite oxides with a chemical formula $\text{Ba}_4\text{MM}'_3\text{O}_{12}$ have been much less explored.

Shimoda *et al.* [26,27] investigated the crystal structure and dc magnetization of $\text{Ba}_4\text{LnM}'_3\text{O}_{12}$ (Ln = rare earth ion;

*Corresponding author: abhisek.ban2011@gmail.com;
abhisek.bandyopadhyay@stfc.ac.uk

†Corresponding author: devashibhai.adroja@stfc.ac.uk

Published by the American Physical Society under the terms of the [Creative Commons Attribution 4.0 International](https://creativecommons.org/licenses/by/4.0/) license. Further distribution of this work must maintain attribution to the author(s) and the published article's title, journal citation, and DOI.

$M' = \text{Ir, Ru}$) without shedding light into their true magnetic ground states. More recently, Nguyen *et al.* studied the new 12L family of hexagonal perovskite oxides $\text{Ba}_4\text{NbM}'_3\text{O}_{12}$ ($M' = \text{Ru, Rh, Ir}$) as potential QSL materials [28,29]. Unlike $\text{Ba}_3\text{MM}'_2\text{O}_9$, where the net magnetic moment of individual $M'_2\text{O}_9$ dimers may be zero due to the prevailing intradimer antiferromagnetic coupling, in $\text{Ba}_4\text{MM}'_3\text{O}_{12}$, the net magnetic moment of individual $M'_3\text{O}_{12}$ trimers cannot vanish. An interesting aspect of the $\text{Ba}_4\text{NbM}'_3\text{O}_{12}$ trimer compounds is that the average valence of Ru/Rh/Ir is 3.67+ without any charge ordering among the crystallographic sites. While the $M' = \text{Ir}$ system of the $\text{Ba}_4\text{NbM}'_3\text{O}_{12}$ family has been suggested to be a potential QSL material via combined dc susceptibility and heat capacity measurements, to date, the true magnetic ground state in the materials with $M' = \text{Ru}$ and Rh has not been disclosed [28,29].

Here we present a comprehensive experimental study by means of electronic, magnetic, thermodynamic, and μSR investigations, on a polycrystalline sample of the trimer rhodate $\text{Ba}_4\text{NbRh}_3\text{O}_{12}$ (BNRO). Our temperature-dependent electrical resistivity and valence band spectroscopy confirm the presence of an energy gap at the Fermi energy (E_F) in BNRO. Despite having significant antiferromagnetic interactions [$\Theta_W \sim -35$ to -45 K between the sizable local Rh moments ($\mu_{\text{eff}} \sim 0.73\text{--}0.8\mu_B/\text{Rh}$)], BNRO evades any kind of magnetic long-range ordering and/or spin-glass freezing down to 50 mK. A very high frustration index, $f = |\Theta_W/T_{\text{min}}| > 800$, arises from the edge-shared equilateral Rh-triangular network in this material. We observe a power-law dependence of the low- T (< 25 K) χ_{dc} data and $M(H)$ isotherm. Furthermore, we observe a remarkable universal scaling relation of the $\chi_{\text{dc}}(T, H)$ and $M(H, T)$ in T/H and H/T , respectively. Our zero-field (ZF) and longitudinal-field (LF) μSR results confirm that the Rh moments in BNRO remain dynamic, with no static magnetic ordering, down to a base temperature of 0.26 K. Our temperature dependent magnetic specific heat (C_m) data show a $\gamma T + \alpha T^2$ form between 0.05 and 2 K, indicating a gapless nature for the spin excitations from a metal-like spinon Fermi surface of the novel QSL ground state in this material.

II. EXPERIMENTAL TECHNIQUES

Polycrystalline samples of $\text{Ba}_4\text{NbRh}_3\text{O}_{12}$ were prepared using a conventional solid-state reaction route. Stoichiometric ratios of the starting materials BaCO_3 , Nb_2O_5 , and Rh_2O_3 (Sigma Aldrich, 99.95%, 99.9%, and 99.8%, respectively) were thoroughly mixed in an agate mortar. The powder was then calcined at 850 °C for 24 h in air. The resulting powder was reground, pressed into pellets, and reannealed in air at several higher temperatures (1000, 1100, and then 1150 °C for 12–24 h at each temperature) with intermediate grindings. The phase purity and crystal structure were determined through powder x-ray diffraction (PXRD) using a Bruker D8 Advance diffractometer with $\text{Cu-K}\alpha$ radiation. The structural refinement was performed by the Rietveld technique using FULLPROF [30]. The chemical homogeneity and cation stoichiometry of the samples were checked by analyzing energy dispersive x-ray (EDX) data collected in a ZEISS GeminiSEM 500 scanning electron microscope (SEM).

Temperature dependent electrical resistivity (ρ versus T) measurements were performed using a standard four-probe method over the temperature range 80–400 K using a Quantum Design (QD) Physical Property Measurement System (PPMS). X-ray absorption spectroscopy (XAS) measurements at the Nb L_3 and Rh L_3 edges were performed at the BL16A beamline of the National Synchrotron Radiation Research Center (NSRRC) in Taiwan. Valence band x-ray photoelectron spectroscopy (VBXPS) measurements were carried out at the Max Planck–NSRRC HAXPES end station at the Taiwan undulator beamline BL12XU at SPring-8, Japan. Measurements were made at room temperature using linearly polarized light with a photon energy of 6.5 keV and an energy resolution of 280 meV, using a MB Scientific A-1 HE analyzer mounted parallel to the polarization direction [31]. To corroborate the HAXPES data, we computed the partial density of states by means of fully relativistic density functional theory (DFT) calculations within the local density approximation (LDA) using the full-potential local-orbital (FPLO) code [32]. The dc magnetic susceptibility was measured using a Quantum Design superconducting quantum interference device (SQUID) vibrating sample magnetometer over the temperature range 2–300 K in applied magnetic fields of up to 60 kOe. The temperature dependence of the specific heat, $C_p(T)$, in applied magnetic fields up to 90 kOe, was measured between 2 and 300 K in a QD-PPMS using a 2τ relaxation method. The specific heat and ac magnetic susceptibility, $\chi_{\text{ac}}(T)$, were also measured between 0.05 and 4 K in a QD Dynacool PPMS.

Zero-field and longitudinal-field μSR measurements on polycrystalline $\text{Ba}_4\text{NbRh}_3\text{O}_{12}$ were performed at the ISIS Neutron and Muon Source, UK, using the MuSR spectrometer. For the μSR measurements a powder sample of $\text{Ba}_4\text{NbRh}_3\text{O}_{12}$ was mounted on a silver holder (99.995% purity) using GE varnish diluted with ethanol. The sample was covered with a thin Ag foil and the sample holder was thermally anchored to a sample stick using high-vacuum silicone grease. A He-3 system was used to cool the sample to 0.26 K. The μSR data were analyzed using the MANTID software package [33].

III. RESULTS AND DISCUSSION

A. Structural characterization and composition verification

The Rietveld refined PXRD pattern (see Fig. 1) of BNRO at 300 K confirms the near single phase nature of the sample, with the $R\bar{3}m$ space group in agreement with an earlier report by Nguyen *et al.* [29]. The refined structural parameters along with the goodness of fit factors are summarized in Table I in Appendix A. Allowing the site occupancy of Nb and Rh atoms in the structural refinement to vary led to a full occupancy for these sites, indicating that the sample has the desired composition of $\text{Ba}_4\text{NbRh}_3\text{O}_{12}$. Introducing deliberate site exchange between Nb and Rh did not improve the refinement, eliminating the possibility of any Nb/Rh antisite disorder in this material within the resolution of the structural determination. The data also show the sample contains small amounts of BaRhO_3 ($\sim 2\%$) and Nb_2O_5 ($< 1\%$). Given that BaRhO_3 is a Pauli paramagnet while Nb_2O_5 is nonmagnetic, and that these two phases occur in very small quantities, neither of these

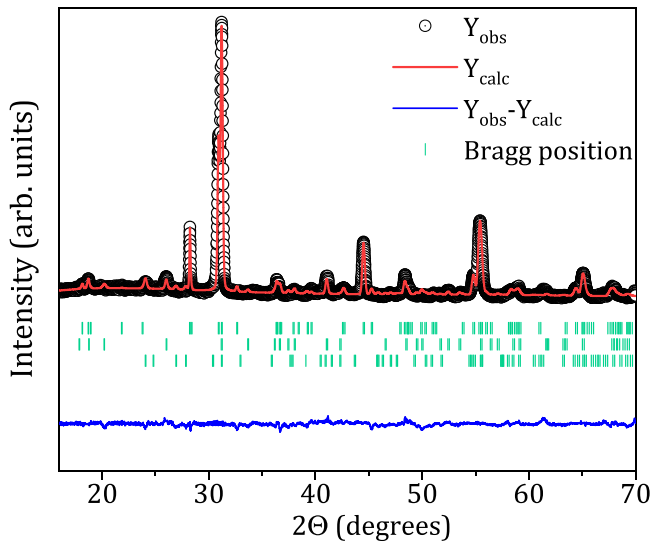


FIG. 1. Rietveld refinement of the powder x-ray diffraction pattern for $\text{Ba}_4\text{NbRh}_3\text{O}_{12}$ at 300 K. The observed (Y_{obs}) and calculated (Y_{cal}) patterns and the difference ($Y_{\text{obs}} - Y_{\text{cal}}$) are shown in black circles and red and blue solid lines, respectively, while the green tick marks denote the allowed peak positions for $\text{Ba}_4\text{NbRh}_3\text{O}_{12}$ (upper row of ticks), BaRhO_3 (middle row ticks), and Nb_2O_5 (lower row of ticks).

two phases should have any influence on the determination of the ground state magnetism of BNRO (see Appendix B).

In agreement with previous work on $\text{Ba}_4\text{NbM}'_3\text{O}_{12}$ systems [28,29], we did not find any evidence of long-range charge ordering (no structural superlattice peaks were observed) within the trimer network of the $\text{Ba}_4\text{NbRh}_3\text{O}_{12}$ material. In addition, SEM-EDX analysis shows that, to within the accuracy of this technique, the sample is chemically homogeneous and the cation stoichiometry is retained at the target composition, i.e., $\text{Ba} : \text{Nb} : \text{Rh} = 19.8(2) : 4.9(1) : 13.8(1) \equiv 4 : 1 : 3$. However, these data cannot rule out the possibility of a variation in the oxygen stoichiometry of the form $\text{Ba}_4\text{NbRh}_3\text{O}_{12-\delta}$.

Figure 2(a) shows the crystal structure consists of three face-sharing RhO_6 octahedra forming Rh_3O_{12} magnetic trimers. Each of the Rh_3O_{12} trimers is connected to its neighboring trimer through corner-sharing nonmagnetic NbO_6 octahedra along the c direction. Such a structural arrangement should naturally give rise to stronger intratrimer Rh-Rh magnetic exchange interactions compared to the intertrimer Rh-Rh exchange couplings via Rh-O-(Nb)-O-Rh super-superexchange interaction pathways. The intratrimer magnetic exchange comprises (i) Rh-Rh direct exchange and (ii) Rh-O-Rh superexchange interaction pathways. The Rh ion has two distinct crystallographic sites in this structure and, consequently, there are two different Rh-O octahedral environments, Rh1O_6 [the middle site in the trimer, shown in Fig. 2(b)] and Rh2O_6 [the two end octahedra of the Rh_3O_{12} trimer, shown in Fig. 2(c)]. As shown in Fig. 2(b), the Rh1 is octahedrally surrounded by six similar oxygen atoms (O1),

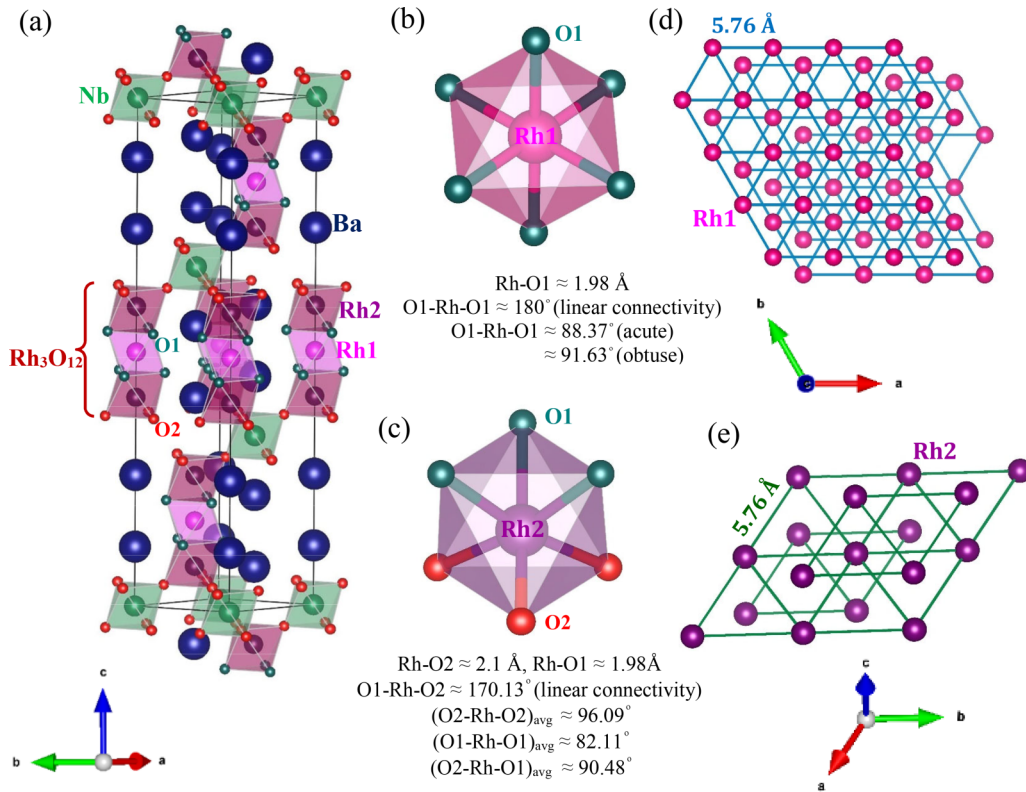


FIG. 2. (a) Refined crystal structure of $\text{Ba}_4\text{NbRh}_3\text{O}_{12}$. The atoms are shown in different colors, while the two distinct types of Rh and O atoms in the Rh_3O_{12} trimer units are labeled. (b), (c) Two distinct RhO_6 octahedra with corresponding Rh-O bond lengths and O-Rh-O bond angles. (d), (e) Edge-sharing equilateral triangular network of Rh ions (shown separately for Rh1 and Rh2 with the Rh-Rh bonds in distinct colors).

resulting in the six identical Rh-O1 bond distances and perfectly linear 180° O1-Rh-O1 connectivity, leading to a nearly undistorted cubic environment. However, the Rh1O₆ octahedra undergo weak trigonal distortion in terms of the deviation of O1-Rh1-O1 bond angles ($\sim 91.6^\circ$) from the ideal 90° expected for cubic symmetry.

On the other hand, as demonstrated in Fig. 2(c), the Rh2 ion is acted upon by local noncubic crystal fields arising from the combined influence of (i) two types of oxygen atoms (O1 and O2) around Rh2 and, correspondingly, two dissimilar Rh2-O bond distances (Rh2-O1 and Rh2-O2), (ii) departure of the linear O1-Rh2-O2 connectivity ($\sim 170.13^\circ$) from perfect 180° , and (iii) rotational distortion around the Rh2O₆ octahedra through the presence of multiple O-Rh2-O bonds (e.g., O1-Rh2-O1, O1-Rh2-O2, and O2-Rh2-O2) and the deviation of each of these bond angles from the ideal 90° of an undistorted octahedra. So, it is quite clear that the Rh-O octahedra host different degrees of local noncubic crystal distortions. This will lead to a difference in the lifting of the Rh- t_{2g} orbital degeneracy locally for the two given Rh-crystallographic sites and, as a result, the local magnetic environments corresponding to the Rh-Rh magnetic superexchange via oxygen will be different for the two Rh sites within the trimers. It is therefore quite reasonable to expect that two-thirds of the Rh₃O₁₂ trimers should exhibit a different magnetic response from that of the remaining third. Lastly, as shown in Figs. 2(d) and 2(e), both the Rh1 and Rh2 ions of the Rh₃O₁₂ trimers separately form edge-sharing equilateral triangle networks in 3D, thus generating a high degree of geometric frustration in BNRO.

B. Electronic characterization

The electrical resistivity, $\rho(T)$, of BNRO increases with decreasing temperature from $\sim 15 \Omega \text{ cm}$ at 400 K, to $\sim 10^5 \Omega \text{ cm}$ at 80 K, where the resistance of the sample then exceeds the limit of the apparatus [see Fig. 3(a)]. The $\rho(T)$ curve follows an Arrhenius activated behavior, with an energy gap of $\Delta \sim 0.32(3) \text{ eV}$ between 240 and 400 K and then undergoes a change in behavior, following a 3D Mott variable-range-hopping mechanism below 240 to 80 K.

The Rh and Nb valences in this system were checked using x-ray absorption spectroscopy at the Nb L_3 and Rh L_3 edges. The results are summarized in Figs. 3(b) and 3(c). We have also measured Nb₂O₅, Sr₂RhO₄, and LaRhO₃ as reference compounds.

For $4d$ transition-metal oxides, the $L_{2,3}$ XAS spectrum basically reflects the unoccupied t_{2g} - and e_g -related peaks in the O_h symmetry due to the larger bandlike character and the stronger crystal field, while the relatively weak intra-atomic multiplet and spin-orbit interactions only modify the relative intensity of the t_{2g} - and e_g -related peaks [34–36]. Figure 3(c) shows the Rh- L_3 XAS spectrum of BNRO, together with Sr₂RhO₄ as a Rh⁴⁺ reference with one hole in the t_{2g} orbitals ($4d^5$) and LaRhO₃ as a Rh³⁺ reference with fully occupied t_{2g} orbitals ($4d^6$). As the energy of the BNRO spectrum lies between those of LaRhO₃ and Sr₂RhO₄, but slightly closer to Sr₂RhO₄, we estimate the Rh valence state of 3.65+ in BNRO, in agreement with the expected average 3.67+ valence of Rh in this material. Another spectral feature indicative of the mixed Rh³⁺ and Rh⁴⁺ valence in BNRO

is the existence of the lower energy shoulder related to an unoccupied t_{2g} peak albeit relatively weak as compared with that in Sr₂RhO₄. As depicted in Fig. 3(b), the Nb- L_3 XAS spectrum of BNRO lies at the same energy as that of Nb₂O₅ indicating a Nb⁵⁺ valence state in the former fulfilling charge balance requirements.

To confirm the gapped electronic nature of this compound, valence band x-ray photoemission data were collected on this material and the results are displayed in Fig. 3(d). The complete absence of any density of states at the Fermi level affirms the insulating behavior of this material. In order to better understand the experimentally collected VBXPS spectrum, we performed density functional theory calculations, with the results shown in Fig. 3(e). The calculated partial density of states (PDOS) in the top panel shows that the O $2p$ bands are widely spread between 8 and 0 eV, while Rh $4d$ has two main features at around 6 and 1 eV, corresponding to the bonding and antibonding from its strong hybridization with the O $2p$ [37]. The Nb $4d$ PDOS is similarly split into two features at a higher binding energy compared to the Rh, as expected from its higher oxidation state. The Ba $5p$ semicore level shows two deep peaks split by SOC, corresponding to the $5p_{3/2}$ and $5p_{1/2}$ contributions, as well as a small amount of weight in the PDOS in the valence region due to weak hybridization to the valence bands.

Our LDA calculations provide a metallic solution, as the O $2p$ -Rh $4d$ bands cross the Fermi energy, indicating the critical role of electron correlations in opening up a gap in this material and, thus, in determining the electronic ground state. Finally, to simulate a spectrum from the PDOS, we multiply each of the PDOS by its photoionization cross section as well as the Fermi function and broaden the result. A rigid shift of 0.8 eV was also applied to take into account the mild effect of correlations. The bottom panel of Fig. 3(e) shows the result of the simulation, which provides a reasonable match to the experiment. The spectral weight of the experimental valence band can be explained mainly by the Rh $4d$ bonding-antibonding peaks, with mixed contributions mainly from the Ba $5p$, which has a very high cross section resulting in its small contributions in the valence region being strongly enhanced [31]. On the other hand, O $2p$, due to very small cross section at high energies, is completely suppressed in the hard x-ray photoemission spectrum.

C. dc and ac magnetizations and universal scaling

The temperature dependence of both zero-field-cooled (ZFC) and field-cooled (FC) dc magnetic susceptibilities in several applied magnetic fields is shown in Figs. 4(a)–4(c) (with data in other fields shown in Appendix C). Rather featureless paramagneticlike dc susceptibility curves are observed in all the applied magnetic fields with no evidence of magnetic ordering and no sign of noticeable thermomagnetic irreversibility (i.e., ZFC/FC divergence) down to 2 K. An M versus H isotherm at 2 K (see Appendix C) also shows no coercivity or remanent magnetization. Furthermore, the temperature dependence of the ac magnetic susceptibility, (χ_{ac}), was measured down to 50 mK at selected frequencies. The real part of the ac susceptibility, $\chi'_{ac}(T)$, shown in Fig. 5 reveals no cusp or peaklike feature, or any noticeable frequency

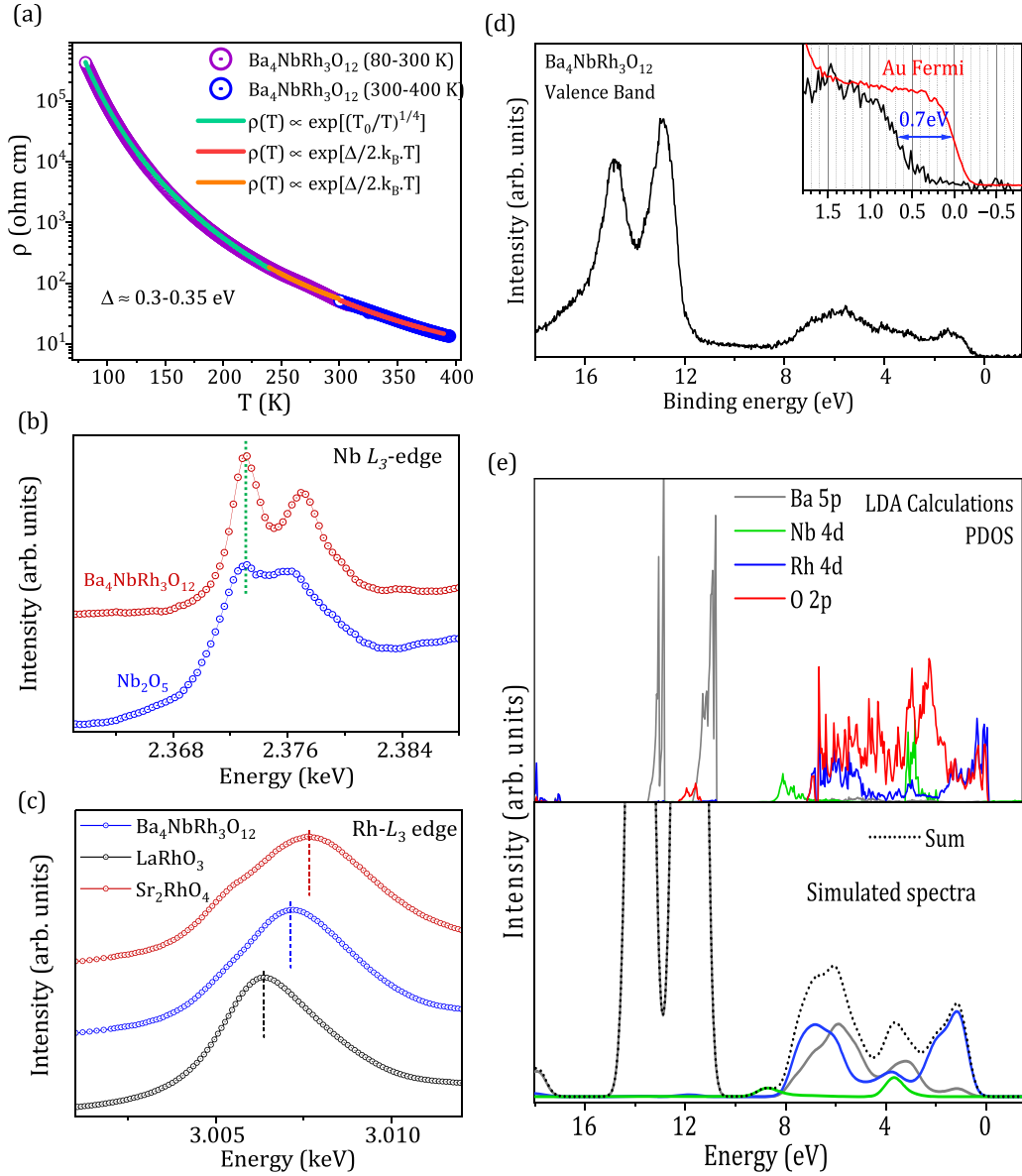


FIG. 3. (a) Temperature dependence of the zero-field electrical resistivity between 80 and 400 K (open colored circles) along with the fits (solid colored lines) in different temperature regions. (b) Nb L_3 -edge XAS spectrum of $\text{Ba}_4\text{NbRh}_3\text{O}_{12}$ along with Nb_2O_5 for comparison. (c) Rh- L_3 edge XAS spectrum for $\text{Ba}_4\text{NbRh}_3\text{O}_{12}$ along with Sr_2RhO_4 and LaRhO_3 for comparison. (d) Valence band photoemission spectrum for $\text{Ba}_4\text{NbRh}_3\text{O}_{12}$. Inset: expanded view of the same near the Fermi energy (solid black line) showing a clear energy gap. The valence band spectrum (solid red line) for gold was measured as a reference to obtain an accurate energy calibration. (e) (Top) Calculated partial density of states (PDOS) of the principal contributions in $\text{Ba}_4\text{NbRh}_3\text{O}_{12}$. (Bottom) Simulated HAXPES valence band spectrum, obtained by multiplying the PDOS of the occupied states shown in the top panel by their respective photoionization cross sections at 6.5 keV photon energy, followed by a broadening to account for experimental conditions, and then their summation.

dependence between 50 mK and 4 K, ruling out a spin frozen magnetic ground state in $\text{Ba}_4\text{NbRh}_3\text{O}_{12}$.

The Curie-Weiss (CW) fit parameters of disordered magnetic systems often depend on the applied magnetic field and the temperature range over which the fits are performed [38]. With this in mind CW fits ($\chi = \chi_0 + \frac{C}{(T - \Theta_W)}$, where χ_0 is a temperature independent susceptibility and C and Θ_W are the Curie constant and Weiss temperature, respectively) were performed on the 5 and 10 kOe FC dc susceptibility data between 100 and 300 K [see Fig. 4(c) and Appendix C]. These fits give an effective magnetic moment, $\mu_{\text{eff}} \sim 0.73-0.8\mu_B/\text{Rh}$

and $\Theta_W \sim -35$ to -45 K, suggesting substantial antiferromagnetic interactions between the Rh moments (see Table II in Appendix C for the CW fit parameters at different temperatures and applied fields). $|\Theta_W|$ is a little higher than an earlier report [29], while a μ_{eff} of $1.48\mu_B/\text{f.u.}$ (or $\sim 0.85\mu_B/\text{Rh}$) in Ref. [29] is close to the value estimated here. Our μ_{eff} per Rh ion is smaller than the spin-only value of $S = 1/2$ ($\approx 1.73\mu_B$) for a $\text{Rh}^{4+} 4d^5$ species. The nonzero μ_{eff} contrasts with the expected nonmagnetic ground state of the Rh_3O_{12} trimers having an average Rh valence of $3.67+$ and a distribution of 16 $4d$ electrons in the $a_{1g}^2 e_g^4 a_{2u}^2 e_u^4 e_g^4$ configuration [28] within

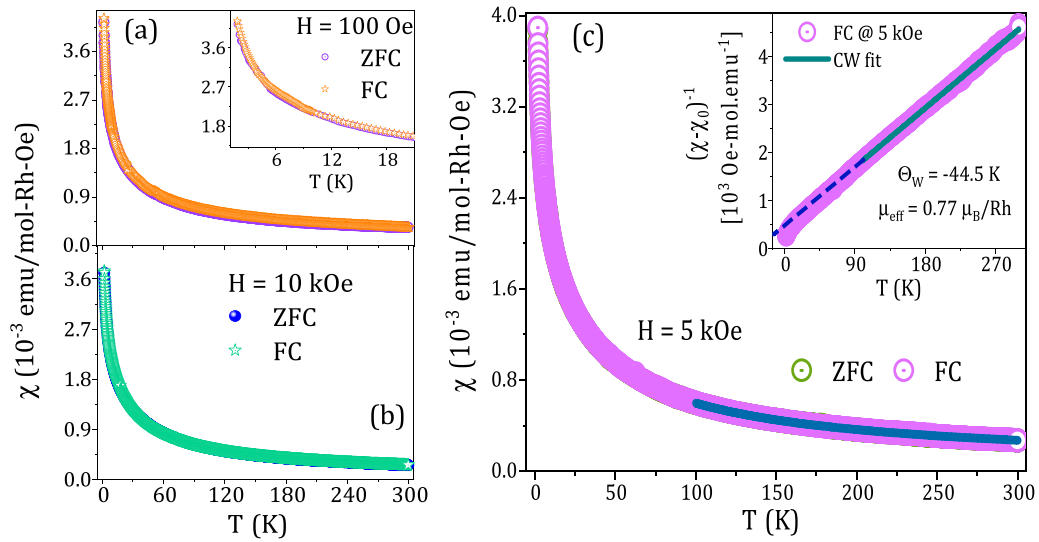


FIG. 4. Zero-field-cooled (ZFC) and field-cooled (FC) dc magnetic susceptibility data as a function of temperature in applied fields of 100 Oe (a) and 10 kOe (b). (c) T dependence of the ZFC and FC dc susceptibility curves in 5 kOe, along with Curie-Weiss fitting (solid cyan line) to the field-cooled susceptibility data. Inset: inverse susceptibility versus temperature along with the linear Curie-Weiss fit.

the Rh₃-only model of the trimer, revealing a deviation from the purely trimer orbital picture in Ba₄NbRh₃O₁₂. Together, these results suggest a delicate balance between SOC, noncubic crystal fields, covalency, and the Rh-Rh direct exchange within the Rh₃O₁₂ trimers [39] in Ba₄NbRh₃O₁₂.

$\chi(T)$ exhibits a power-law behavior, $\chi(T) \sim T^{-\alpha_s}$, where $\alpha_s = 0.34$ at 100 Oe, and then gradually decreases with increasing H , reaching $\alpha_s = 0.2$ for 30 kOe, instead of having a Curie tail, at $T < 25$ K (see Appendix C). Such behavior indicates finite spin degrees of freedom and eliminates the possibility of extrinsic paramagnetic impurities being at the origin of the observed magnetic behavior observed in this material [40,41]. The 2 K $M(H)$ curve also shows a power-law dependence, $M(H) \sim H^{1-\alpha_m}$ with $\alpha_m = 0.32$ [see inset to Fig. 6(b)], over almost the entire measured field range. Such a power-law behavior in both $\chi(T)$ and $M(H)$ with $\alpha_s \approx \alpha_m$

constitutes a signature characteristic of a spin-liquid/valence-bond/random-singlet [40–44]. Further, to check the validity of dynamical scaling behavior, we plot $H^{\alpha_s} \chi_{dc}(T)$ versus T/H and $T^{\alpha_m-1} M(H)$ versus H/T in Figs. 6(a) and 6(b), respectively. Significantly, the (H, T) -dependent χ_{dc} data [Fig. 6(a)] overlap over nearly four orders of magnitude in the T/H with the same value of $\alpha_s = 0.3$. As shown in Fig. 6(b), a similar scaling is seen in the $M(H)$ isotherms (up to $H = 60$ kOe) at different temperatures (2, 5, 10, and 50 K), where the $T^{\alpha_m-1} M(H)$ versus H/T curves with $\alpha_m = 0.32$ collapse onto a single scaling curve. The scaling exponent of 0.3–0.32 for the two distinct thermodynamic quantities $\chi(T)$ and $M(H)$ agree exceptionally well, mirroring with the universal scaling relation of frustrated quantum magnets featuring a QSL phase [40–42,45].

D. Muon-spin-rotation/relaxation (μ SR)

To gain further insights into the magnetic ground state and the nature of local spin dynamics in BNRO, we employed the μ SR technique, which is a highly sensitive microscopic local magnetic probe to detect small static local fields (of the order of 0.1 Oe) arising from long-range order or spin freezing.

Zero-field μ SR measurements were carried out down to 0.26 K with the results shown in Fig. 7(a). The absence of coherent spontaneous oscillations and/or a $\frac{2}{3}$ drop in the initial muon asymmetry rules out any static long-range magnetic order down to 0.26 K in BNRO. The ZF- μ SR asymmetry curves from 50 to 0.26 K have been fit satisfactorily using a combination of a simple exponential decay and a stretched exponential relaxation function,

$$A(t) = A_{\text{bkg}} + A_1 \exp(-\lambda_1 t)^\beta + A_2 \exp(-\lambda_2 t). \quad (1)$$

The first term in Eq. (1) accounts for the time independent background from the muons stopping in the silver sample holder. A_{bkg} was estimated by fitting the data at 0.26 K and was then kept fixed at 0.052 throughout the ZF data analysis.

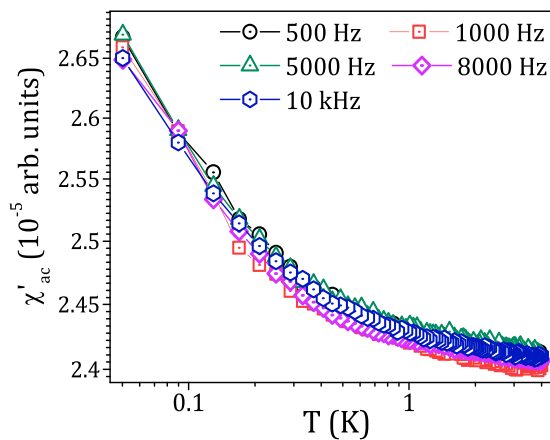


FIG. 5. Temperature dependence of the real part of ac magnetic susceptibility χ'_{ac} on a log-log scale between 0.05 and 4 K at selected frequencies $\nu = 0.5, 1, 5, 8,$ and 10 kHz, with an ac excitation field $H_{ac} = 1$ Oe and no dc-applied field.

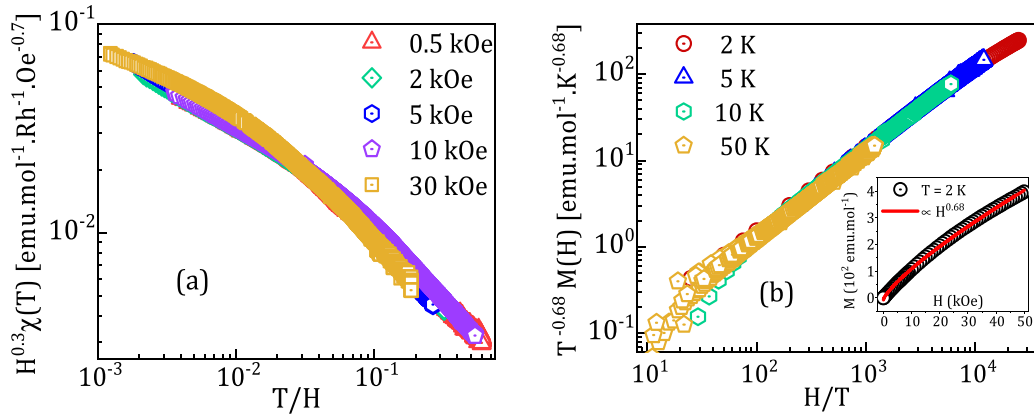


FIG. 6. (a) Scaling of $H^{0.3} \chi_{dc}(T)$ with T/H on a log-log scale. (b) Log-log scaled plot of $T^{-0.68} M(H)$ versus H/T . Inset: $M - H$ isotherm at 2 K (shown only for the first quadrant) along with a power-law fit, $M(H) \propto H^{1-\alpha_m}$ with $\alpha_m \equiv 0.32$.

The second and third terms model fast and slowly relaxing components corresponding to two different muon stopping sites, which are likely to be related with the two crystallographically inequivalent Rh sites and the resulting dissimilar oxygen coordination environments within the Rh_3O_{12} trimer of the 12L structure (see Fig. 2 and details of the structure). λ_1 , λ_2 , and A_1 , A_2 are the relaxation rates and the relative weight

fractions of the muon asymmetry amplitude of the fast and slow relaxing parts, respectively. The total muon asymmetry is fixed at ~ 0.25 , while the values of A_1 and A_2 remain nearly unchanged at ~ 0.13 and ~ 0.067 , respectively, throughout the T range of the ZF measurements. Based on the obtained asymmetry amplitudes A_1 and A_2 , the development of fast and slow relaxing components can roughly be ascribed to the

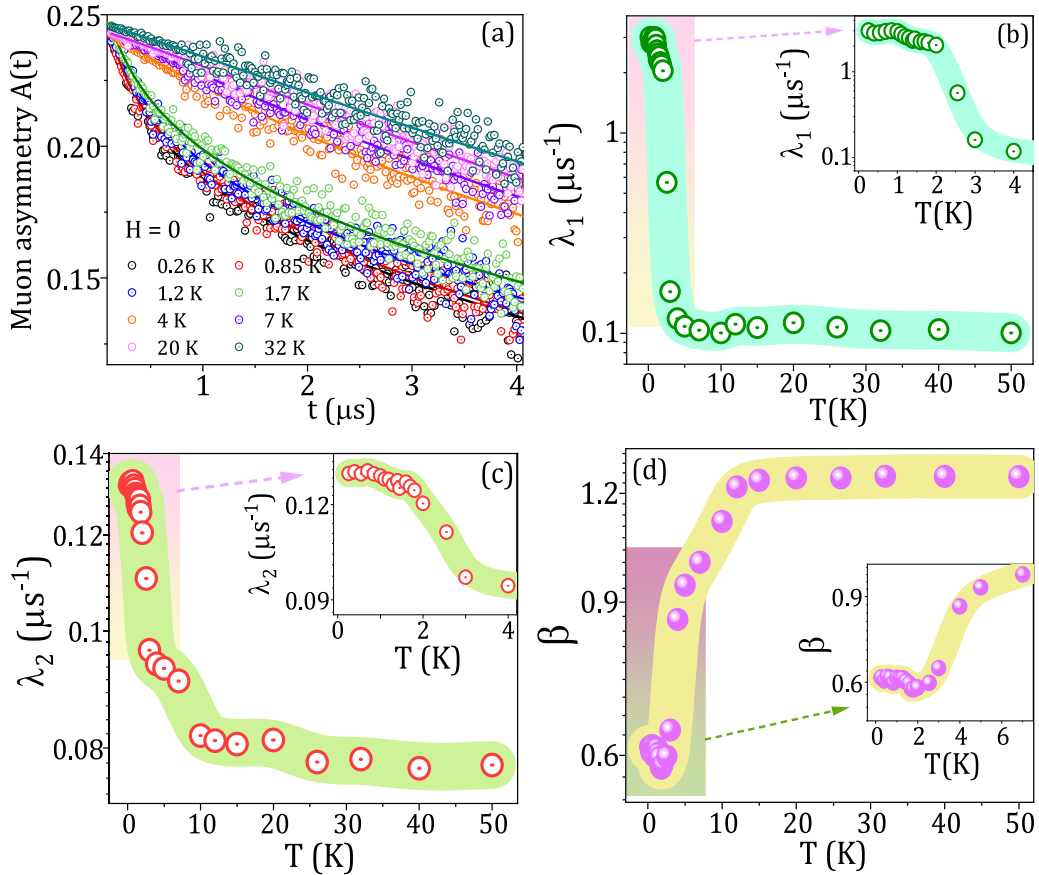


FIG. 7. (a) Time evolution of the zero-field muon asymmetry curves at selected temperatures. Temperature dependence of the (b) fast and (c) slow relaxation rates and (d) the stretched exponent associated with λ_1 , shown on log-linear scales to enhance the clarity of the presentation. Insets show views over a reduced temperature window. The uncertainties on the experimental data points in (a) and the fitting parameters (λ_1 , λ_2 , and β) are all below 2% and so are not shown for clarity. The broad shaded lines in (b), (c), and (d) are guides to the eye.

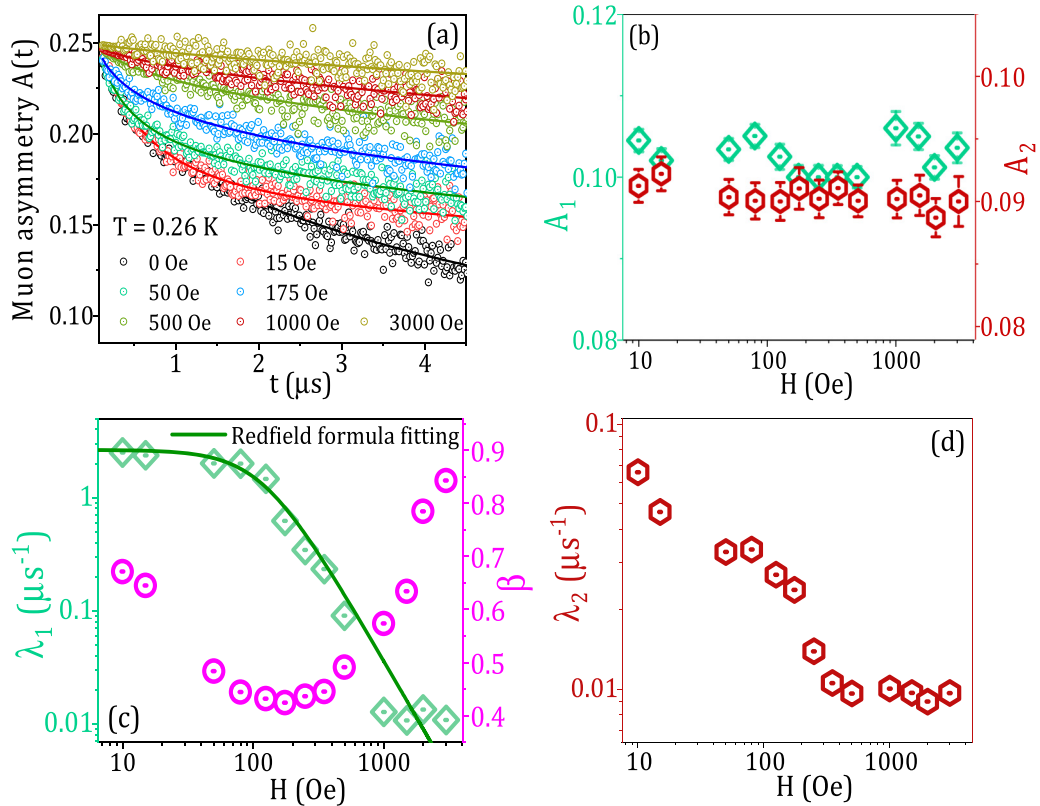


FIG. 8. (a) Time evolution of the muon asymmetry at the base temperature $T = 0.26$ K in longitudinal applied fields. (b) Variations of the muon asymmetry amplitude for the fast relaxing component (left y axis) and the slow relaxing part (right y axis) as a function of applied longitudinal field (LF) on a log-linear scale. (c) Longitudinal field (LF) dependence of the fast relaxation rate (left y axis) and its associated stretched exponent (right y axis) on a log-log and linear-log scale, respectively. (d) Log-log scale plot of the longitudinal field dependence of the slow relaxation rate. Log scales are employed to better illustrate the field dependence of the data.

contributions from distinct local internal fields corresponding to, respectively, the two-thirds (Rh₂O₆ at the ends) and one-third (Rh₁O₆ in the middle) of the Rh₃O₁₂ trimer units. We support our two-component μ SR fitting model by considering the distribution of muon-spin relaxation rates around the more inhomogeneous Rh2 site (two sets of Rh-O distances, a departure of the O1-Rh2-O2 bond angle from linear 180°, and the presence of stronger trigonal distortion in light of larger deviation of the O-Rh2-O bond angles from 90° of ideal cubic) that would naturally give rise to stretched exponential relaxing component $A_1 \exp(-\lambda_1 t)^\beta$, while a nearly undistorted local octahedral environment around the Rh1-site (six identical Rh-O distances and perfect linear 180° O1-Rh1-O1 connectivity) would offer a simpler exponential relaxation $A_2 \exp(-\lambda_2 t)$. As shown in Fig. 7(a), the asymmetry curves do not change appreciably from the measurement at lowest temperature, $T = 0.26$ K, to about 2 K, and upon further increase in temperature the muon spin relaxation starts to gradually decrease. As illustrated in Figs. 7(b) and 7(c), the relaxation rates, λ_1 and λ_2 , of the fast and slow relaxing components, respectively, remain nearly constant ($\lambda_1 \sim 0.1 \mu\text{s}^{-1}$ and $\lambda_2 \sim 0.07\text{--}0.08 \mu\text{s}^{-1}$) in the temperature range of 50 to 10 K, in agreement with the paramagnetic fluctuations [22] of Rh local moments. Between ~ 5 and 2 K, the relaxation rates λ_1 and λ_2 gradually increase with decreasing temperature, indicating a slowing down of the Rh-spin fluctuations, as commonly observed in other QSL materials [22,46–49]. Despite such an obvious slowing down

of the spin dynamics there is no static long-range magnetic order in this system as inferred from the absence of diverging relaxation rate at lowest temperature [see Figs. 7(b) and 7(c)]. Rather, upon further cooling below 2 K, both λ_1 and λ_2 level off ($\lambda_1 \sim 2.9 \mu\text{s}^{-1}$ and $\lambda_2 \sim 0.135 \mu\text{s}^{-1}$) and maintain a nearly temperature-independent plateaulike behavior between 2 and 0.26 K. This suggests the persistence of strong quantum spin fluctuations [22,46–50]. The exponent, β , of the fast relaxation gradually decreases on lowering the temperature, reaching an almost constant value of ~ 0.6 between 2 and 0.26 K [see Fig. 7(d)]. Here, β is larger than the $\beta = 1/3$ of a canonical spin glass [51], making it less likely that any spin freezing is associated with the fast relaxation in the ground state.

Muon decoupling experiments were performed in several applied longitudinal fields at 0.26 K and the results are shown in Fig. 8(a). The LF- μ SR data were fit using Eq. (1), where A_{bkg} is fixed at the ZF value of 0.052 and A_1 and A_2 remain nearly independent of the applied longitudinal fields [see Fig. 8(b)]. As shown in Figs. 8(a), 8(c), and 8(d), the relaxation rates of both the fast and slow relaxing components gradually decrease with increasing applied LF. There is a significant decoupling of the muons from the local internal fields at moderate applied LFs; however, there is still some relaxation at the highest applied LF of 3000 Oe [see Fig. 8(a) and also the λ_i ($i = 1, 2$) versus H variations in Figs. 8(c) and 8(d)]. If the muon depolarization arises from

any static internal magnetic field of width ΔH_i , the zero-field muon relaxation rates, $\lambda_1 \approx 2.9 \mu\text{s}^{-1}$ (fast relaxation) and $\lambda_2 \approx 0.135 \mu\text{s}^{-1}$ (slow relaxation) obtained from the ZF μSR data analysis at the lowest measured temperature, would suggest an estimated static field ($\Delta H_i \simeq 2\pi\lambda_i/\gamma_\mu$, where γ_μ is the muon gyromagnetic ratio) of about $\Delta H_1 \approx 21.3$ Oe and $\Delta H_2 \approx 1$ Oe. It may then be anticipated that an applied longitudinal field of $5\Delta H_i$ to $10\Delta H_i$ would completely suppress that static internal field and, consequently, completely decouple the muon spins from the influence of the static moments/fields [22,48,49,52,53]. Here we applied longitudinal fields up to 3000 Oe, which is about 140 and 3000 times larger than $\Delta H_1 \approx 21.3$ Oe and $\Delta H_2 \approx 1$ Oe, respectively, yet astonishingly there is no sign of full suppression of the muon depolarization. This corroborates the existence of strongly fluctuating Rh spins down to at least 0.26 K in $\text{Ba}_4\text{NbRh}_3\text{O}_{12}$.

The field dependence of the relaxation rates was analyzed using the Redfield formula [54]:

$$\lambda_{\text{LF}}(H) = \frac{2\gamma_\mu^2 \langle H_{\text{loc}}^2 \rangle \nu}{\nu^2 + \gamma_\mu^2 H_{\text{LF}}^2}. \quad (2)$$

Here ν is the fluctuation rate (related to the correlation time $\tau = 1/\nu$), H_{loc} is the time average of the fluctuating amplitude of local internal field, and H_{LF} is the applied LF field. As shown in the semilog plot of Fig. 8(c), λ_1 is well described with the Redfield formula, while λ_2 is not, because of the double-step-like structure at lower fields [see Fig. 8(d)]. The inadequacy of the Redfield formula in describing the LF dependence of λ_2 (the slowly relaxing component) possibly suggests the development of some more complex additional spin correlations and therefore warrants future investigations. The parameters estimated from the fit to $\lambda_1(H)$ [Fig. 8(c)] using Eq. (2) are $H_{\text{loc}} \approx 42$ Oe and $\nu = 9.98$ MHz. As demonstrated in Fig. 8(c) (right y axis), the stretched exponent β of the fast relaxing component initially decreases and exhibits a minimum near 200 Oe and then monotonically increases with field and gradually approaches close to 1 with increasing applied LF.

E. Specific heat

The extent of magnetic frustration in any magnetically disordered material is inevitably reflected through the amount of retained magnetic entropy within that system at very low temperature. To investigate the magnetic ground state and the nature of low-energy spin excitations in this compound, we have measured the temperature dependence of the specific heat (C_p) from 0.05 to 200 K in both zero and several applied magnetic fields.

Taking the lattice contribution to the total C_p to be negligible in the temperature range 0.05–4 K, we assume $C_p \approx C_m$, the magnetic specific heat, in this low temperature region. $C_p(T)$ from 2 to 200 K [Fig. 9(a)] and C_m versus T between 0.05 and 4 K [Fig. 9(c)] show no sharp λ -like anomaly, supporting the absence of a thermodynamic phase transition to a long-range magnetically ordered state and/or a structural phase transition.

After subtracting the lattice contribution, C_L , from the specific heat between 2 and 200 K (see Appendix D for details

of how C_L was estimated), we combine the result with the 0.05–4 K $C_m(T)$ data in order to illustrate the temperature dependence of the magnetic specific heat over the entire measured T range. The magnetic specific heat $C_m(T)$ [Fig. 9(b)] reveals a weak but noticeable field dependence below ~ 10 K, indicating short-range magnetic correlations. Furthermore, C_m exhibits a broad, strictly field-independent maximum around 28–32 K, suggesting a highly frustrated nature for the magnetic interactions in $\text{Ba}_4\text{NbRh}_3\text{O}_{12}$, as seen in several reported spin liquids [5,55,56]. The release of magnetic entropy S_m [inset to Fig. 9(b)] in zero field, obtained by integrating $\frac{C_m}{T}$ with respect to T , gives only $\approx 25\%$ of the maximum $R \ln 2$ (5.76 J/mol K²) for a completely ordered magnetic state. This points towards the retention of a large percentage of magnetic entropy, indicating the presence of persistent spin fluctuations and also low-energy spin excitations in this system [9,29,46,57,58].

Focusing on the data from 0.05 to 4 K, an upturn is evident in the zero-field $C_m(T)/T$ data [see inset to Fig. 9(a)], which is systematically weakened by the application of a magnetic field, a common occurrence in many QSL materials [29,57–61]. As shown in Fig. 9(c), $C_m(T)/T$ in both zero field and applied fields has a negative $\log(T)$ dependence with decreasing temperature and then exhibits a peaklike feature at ~ 2.45 K. This might suggest the emergence of a quantum critical region [62,63]. The observed anomaly is unaltered by the application of applied fields and so could not be ascribed to a two-level Schottky anomaly effect due to paramagnetic impurity spin centers. As our combined dc, ac magnetizations and μSR data indicate that there is no static magnetic ordering down to at least 0.05 K, it is also very unlikely this anomaly in $C_m(T)/T$ is the result of any magnetic ordering. Instead, one explanation could be the dominance of magnetic fluctuations in the low- T heat capacity. On the other hand, this peak may be indicative of a crossover from a thermally disordered paramagnetic to a quantum disordered spin-liquid phase [22,47,52,56,64]. Note that this anomaly occurs in a similar temperature range to the T -independent plateaulike behavior in the ZF μSR relaxation rates. All these points indicate the emergence of a low-temperature dynamic QSL phase.

In order to obtain a deeper understanding of the nature of low-energy spin excitations in the ground state of BNRO, the $C_m(T)$ data between 0.05 and 2 K, with and without magnetic fields [see Fig. 9(d)], were analyzed using

$$C_m = \gamma T + \alpha T^2 + f C_{\text{Sch}}, \quad (3)$$

where f represents the number of paramagnetic impurity centers, while $C_{\text{Sch}} = R \left(\frac{\Delta}{k_B T}\right)^2 \frac{\exp(\Delta/k_B T)}{[1 + \exp(\Delta/k_B T)]^2}$ denotes a standard two-level Schottky contribution, corresponding to $f\%$ of free spins. Δ/k_B defines the two-level Schottky energy gap. γ in Eq. (3) is an anomalous linear term representing the Sommerfeld coefficient typically observed in metals. Fitting yields an f value of $\sim 1.4\%$, which implies a very small proportion of impurity free-spin centers in the sample, in line with the structural and EDX characterization. As shown in Fig. 9(f), the Schottky energy gap Δ/k_B varies linearly with H and the estimated g value of 1.8 matches quite well with the ideal Landé- g factor, $g = 2$, for an $S = 1/2$ spin of a $4d^5$ Rh⁴⁺

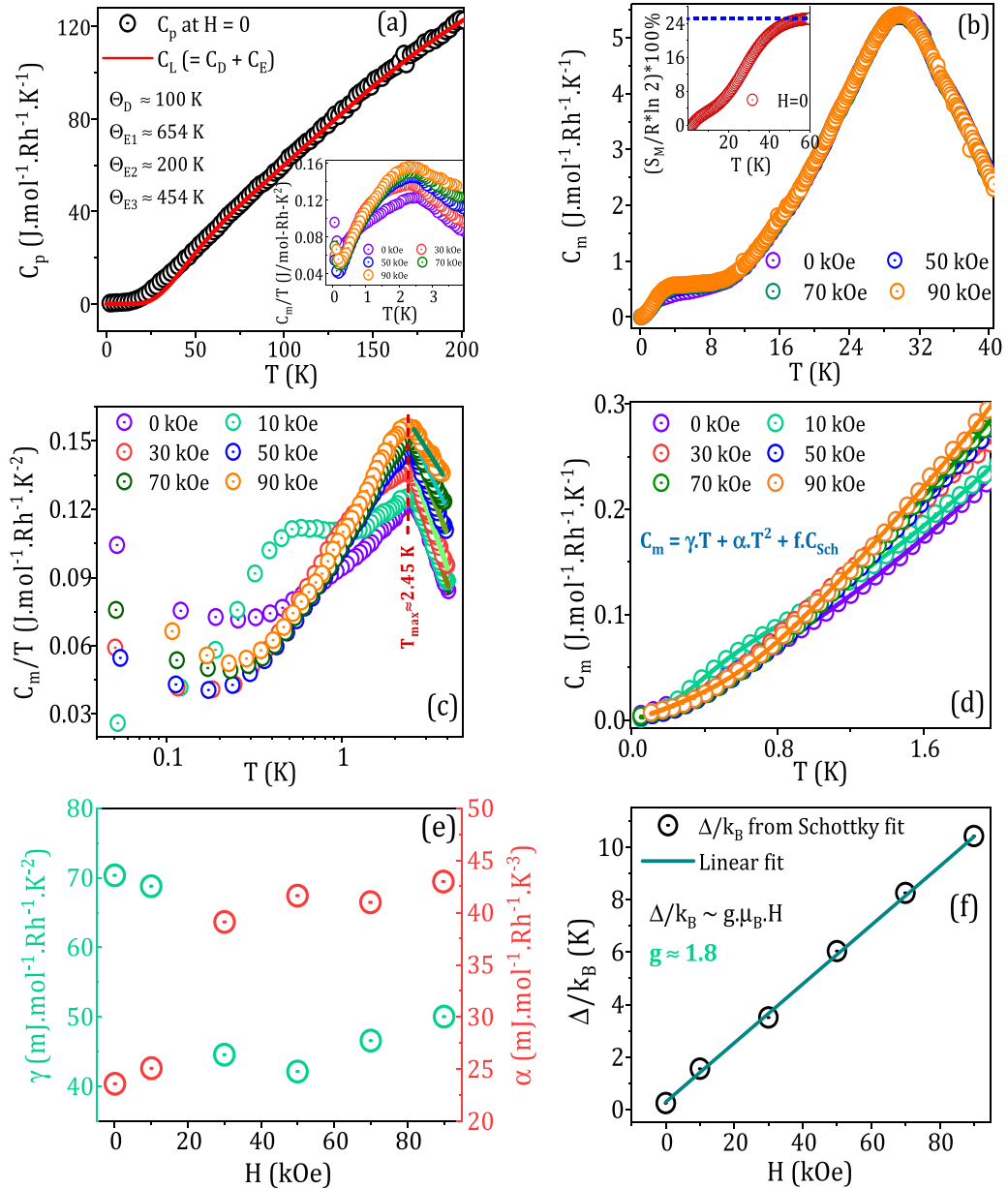


FIG. 9. (a) Temperature dependence of the total specific heat C_p between 2 and 200 K for $H = 0$ (open black circles) and the lattice contribution (solid red line) estimated using a Debye-Einstein model. Inset: C_m/T versus T curves in both the zero and several applied magnetic fields between 0.05 and 4 K. (b) Temperature dependence of the magnetic specific heat C_m and zero-field magnetic entropy S_m (top left inset); (c) C_m/T versus $\log(T)$ plots along with the respective linear fits (solid colored lines) for $2.5 \leq T \leq 4$ K. (d) Temperature dependent magnetic specific heat C_m data in the range 0.05–2 K for different applied fields, along with the respective fits (solid colored lines). (e) The variation of the coefficients of linear (green open circles; left y axis) and quadratic (red open circles; right y axis) terms is shown as a function of applied H . (f) Schottky energy gap versus applied field and the corresponding linear fit.

ion. This small fraction of paramagnetic Rh^{4+} centers might arise from the $\text{BaRh}^{4+}\text{O}_3$ secondary phase. It is quite clear that such a low fraction of paramagnetic Rh^{4+} impurities cannot explain either the intriguing low- T magnetic specific heat or the magnetic response of this material. Rather, the resulting ground state magnetic and thermodynamic behaviors are governed by the $\text{Ba}_4\text{NbRh}_3\text{O}_{12}$ phase.

The fits reveal that C_m has a linear T dependence in all the measuring fields, which together with the large γ [$\gamma_{\text{avg}} \approx 70 \text{ mJ mol}^{-1} \text{K}^{-2}$ for $H \leq 10$ kOe and $\approx 45 \text{ mJ mol}^{-1} \text{K}^{-2}$ for $H \geq 30$ kOe, as shown in Fig. 9(e)]

are unusual for charge-gapped spin-orbit Mott insulators and signify low-lying gapless spin excitations from a metal-like spinon Fermi surface. In other words, the presence of a finite γ in $\text{Ba}_4\text{NbRh}_3\text{O}_{12}$ could suggest the fractionalization of electrons and a persistent metal-like spinon Fermi surface, as discussed in the context of a gapless QSL ground state [5,17,50,65–69]. The γ in BNRO is substantial and contrasts with the small γ values found in disordered insulators such as TiO_2 ($\sim 0.1 \text{ mJ/mol K}^2$ [70]), but is comparable with those reported in other gapless QSL candidates, such as $\text{Ba}_3\text{CuSb}_2\text{O}_9$ (43.4 mJ/mol K^2)

[71], $\text{Ba}_3\text{ZnIr}_2\text{O}_9$ (25 mJ/mol K^2) [17], Ba_2YIrO_6 (44 mJ/mol K^2) [65], $\text{Ba}_3\text{NiIr}_2\text{O}_9$ (45 mJ/mol K^2) [52], $\text{Sr}_2\text{Cu}(\text{Te}_{0.5}\text{W}_{0.5})\text{O}_6$ (54.2 mJ/mol K^2) [58], $\text{EtMe}_3\text{Sb}[\text{Pd}(\text{dmit})_2]_2$ (20 mJ/mol K^2) [72], and herbertsmithite $\text{ZnCu}_3(\text{OH})_6\text{Cl}_2$ (33–50 mJ/mol K^2) [73].

At very low T , C_m also exhibits a significant T^2 dependence, with $\alpha_{\text{avg}} \approx 25$ mJ/mol K^3 for $H \leq 10$ kOe and ≈ 40 mJ/mol K^3 for $H \geq 30$ kOe [see Fig. 9(e)], which is common in the spin-orbit coupled heavier $4d$ and $5d$ transition metal based quantum magnets as a fingerprint of a gapless QSL ground state [74–77]. The notable changes in both γ and α shown in Fig. 9(e) in applied fields $H > 10$ kOe may be a topic for future in-depth high-field μSR studies. Only a combined $\gamma T + \alpha T^2$ fit gives a satisfactory agreement with each $C_m(T)$ data set between 0.05 and 2 K. The quadratic dependence may result from novel Dirac QSL phenomenology in terms of so-called Dirac spinon excitations with linear dispersion, similar to that recently reported in $\text{Sr}_3\text{CuSb}_2\text{O}_9$ [48] and $\text{YbZn}_2\text{GaO}_5$ [78]. Such a T^2 dependence is often seen in frustrated quantum magnets that follow a power-law scaling with a data collapse of the thermodynamic quantities in the dimensionless entities T/H and H/T [40,42]. However, unlike the universal scaling relation for $\chi(T)$ and $M(H)$ discussed above, the $C_m[T, H]/T$ data for $\text{Ba}_4\text{NbRh}_3\text{O}_{12}$ do not show a power-law scaling [Fig. 9(c)] and data collapse in T/H [see Fig. 10(b) in Appendix C for the scaling exponent $\alpha = 0.31$], implying additional low-lying excitations, as previously reported in the case of the candidate Kitaev QSL material Cu_2IrO_3 [40].

IV. CONCLUSION

Our in-depth dc and ac magnetic susceptibility, magnetic specific heat, and muon-spin-rotation/relaxation investigations point towards the stabilization of a gapless quantum spin liquid ground state in this trimer based mixed-valent $4d$ rhodate $\text{Ba}_4\text{NbRh}_3\text{O}_{12}$. Despite significant antiferromagnetic interactions between the sizable Rh-local moments, BNRO does not exhibit any static magnetic ordering, instead showing the presence of continuously fluctuating dynamic Rh moments down to 50 mK, which is well below the Θ_W of -35 to -45 K. The edge-shared equilateral Rh triangular network exerts strong geometric exchange frustration, which facilitates enhanced quantum fluctuations among the Rh moments and, hence, stabilizes a dynamic QSL ground state. The magnetic specific heat reveals a significant T -linear plus T^2 dependence. The former suggests gapless spin excitations in this charge-gapped insulator, while the latter may indicate the presence of Dirac spinons with linear dispersion. The Rh L_3 -edge x-ray absorption spectroscopy confirms the Rh valence to be in agreement with the expected average $3.67+$ in this material. Our work offers new material directions to explore in the field of QSLs, within the relatively unstudied moderately spin-orbit coupled $4d$ family of rhodates.

ACKNOWLEDGMENTS

A.B. and D.T.A. would like to thank Professor L. H. Tjeng, Professor A. Severing, Professor G.-L. Pascut, Dr. A. Yogi, Dr. M. Isobe, Dr. M. Gutmann, and Dr. R. Perry for inter-

esting discussions. A.B. and D.T.A. thank the EPSRC UK for the funding (Grant No. EP/W00562X/1). D.T.A. would like to thank the Royal Society of London for International Exchange funding between the UK and Japan, and Newton Advanced Fellowship funding between the UK and China. The authors acknowledge the Materials Characterization Lab (MCL) of ISIS facility, UK for providing experimental facilities. The authors also thank the ISIS facility for the beam time RB2010177 [79].

APPENDIX A: STRUCTURAL PARAMETERS OBTAINED FROM A RIETVELD REFINEMENT OF PXRD DATA

Table I gives the structural information extracted from the Rietveld refinement of the powder x-ray diffraction data at 300 K for $\text{Ba}_4\text{NbRh}_3\text{O}_{12}$ shown in Fig. 1.

APPENDIX B: VALIDATION OF INTRINSIC MAGNETISM

The measured dc magnetic susceptibilities and the resulting CW fit parameters are consistent among the different batches of this material and with the specific-heat measurements discussed above. If one insists on claiming that bulk $\text{Ba}_4\text{NbRh}_3\text{O}_{12}$ is nonmagnetic and the observed magnetic moments ($\mu_{\text{eff}} \sim 0.73\text{--}0.8\mu_B/\text{Rh}$) arise from extrinsic impurities, this would require roughly 26% of a spin-1 $\text{Rh}^{5+} 4d^4$ or $\sim 43\%$ of a spin-1/2 $\text{Rh}^{4+} 4d^5$ impurity, both of which are orders of magnitude larger than the impurity levels found in our structural characterization. Furthermore, the temperature independent paramagnetic susceptibility, estimated from the CW fitting, is $\chi_0 \sim 5 \times 10^{-5}$ emu/mol Oe, which is orders of magnitude smaller than that reported for BaRhO_3 ($\sim 10^{-3}$ emu/mol Oe) [80]. In addition, given that the effective magnetic moment in BaRhO_3 , μ_{eff} , is $\sim 0.27\mu_B/\text{Rh}$, $\sim 3\%$ of BaRhO_3 impurity in our $\text{Ba}_4\text{NbRh}_3\text{O}_{12}$ compound would only result in $\sim 0.01\mu_B$ per Rh, much smaller than the value obtained from our CW fit. The Weiss temperature, $\Theta_W \sim -10$ K, of the Pauli paramagnet BaRhO_3 [80] is also considerably lower than those of $\text{Ba}_4\text{NbRh}_3\text{O}_{12}$ estimated in the present work. All these factors support the intrinsic nature of bulk magnetism in our $\text{Ba}_4\text{NbRh}_3\text{O}_{12}$ sample.

APPENDIX C: ADDITIONAL MAGNETIC CHARACTERIZATION DATA

Magnetization versus field isotherms between 2 and 250 K [Fig. 10(a)] reveal paramagnetic behavior. Figure 10(b) shows the scaling behavior of the magnetic specific heat at various applied magnetic fields. Our analysis reveals deviations from a universal scaling behavior in the $H^\alpha C_m/T$ versus T/H data with a scaling exponent $\alpha_s = 0.31$. Figure 11 shows the temperature dependent zero-field-cooled and field-cooled dc magnetic susceptibility at various applied magnetic fields. The fit parameters obtained from the analysis of the susceptibility are given in Table II. Figure 12 shows the power-law behavior of the dc magnetic susceptibility at low temperature.

TABLE I. Structural information extracted from the Rietveld refinement of the powder x-ray diffraction data at 300 K of $\text{Ba}_4\text{NbRh}_3\text{O}_{12}$. Space group: $R\bar{3}m$, $a = b = 5.7631(6)$ Å, $c = 28.4649(9)$ Å, $\gamma = 120^\circ$, $V = 811.103(11)$ Å³; $R_p = 7.56$, $R_{wp} = 10.95$, $R_{exp} = 7.64$, $\chi^2 = 2.05$. B is the isotropic temperature factor.

Atom	Site	Occupancy	x	y	z	B (Å ²)
Ba1	6c	1.000	0	0	0.11669(15)	0.006(26)
Ba2	6c	1.000	0	0	0.25776(18)	0.0068(30)
Nb	3a	1.000	0	0	0	0.0095(38)
Rh1	3b	1.000	0	0	0.5	0.0085(18)
Rh2	6c	1.000	0	0	0.41064(16)	0.0085(18)
O1	18h	1.000	0.4929(18)	0.5071(20)	0.1254(14)	0.015(32)
O2	18h	1.000	0.5072(22)	0.4988(15)	0.2918(21)	0.015(32)

APPENDIX D: ESTIMATE OF THE LATTICE CONTRIBUTION C_L TO THE SPECIFIC HEAT

$C_p(T)$ between 2 and 200 K is modeled by the sum of the lattice (C_L) and magnetic (C_m) contributions, as the presence of any two-level Schottky anomaly effect due to paramagnetic

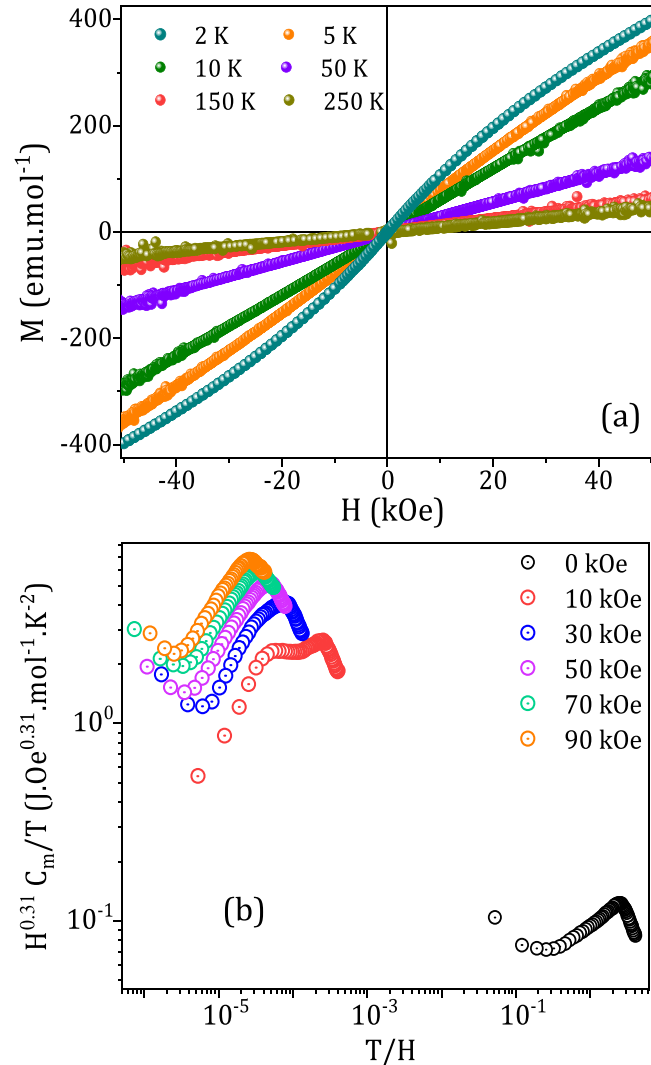


FIG. 10. (a) $M(H)$ isotherms at selected temperatures. (b) Deviations from the universal scaling behavior in the $H^{\alpha_s} C_m/T$ versus T/H data with the scaling exponent $\alpha_s = 0.31$.

impurity centers has been found to be negligible from a two-level Schottky anomaly analysis (not shown) in the 2–20 K C_p data. In the absence of a suitable nonmagnetic analog, C_L was estimated by fitting the high-temperature (65–200 K) C_p data using a Debye-Einstein model with a combination of one

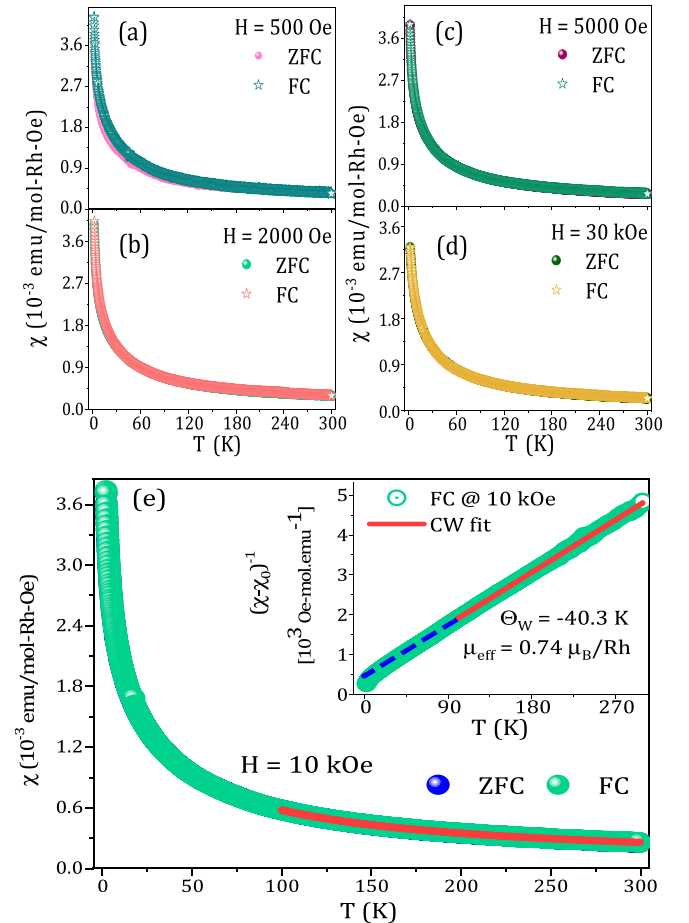


FIG. 11. Temperature dependent zero-field-cooled and field-cooled dc magnetic susceptibility curves in (a) 500 Oe, (b) 2000 Oe, (c) 5000 Oe, and (d) 30 kOe applied fields. (e) T dependence of zero-field-cooled and field-cooled 10 kOe dc susceptibility curves along with Curie-Weiss fitting (solid red line). Inset: respective inverse susceptibility versus temperature plot along with linear CW fit (solid red line), where the extended dashed blue line down to the lowest temperature shows a departure from the CW fit.

TABLE II. Parameters obtained from fitting the dc magnetization data to a Curie-Weiss law over two temperature ranges in several applied magnetic fields for $\text{Ba}_4\text{NbRh}_3\text{O}_{12}$. The R^2 values indicate the goodness of the fits.

T range (K)	H (kOe)	Θ_W (K)	μ_{eff} (μ_B/Rh)	$\chi_0 \times 10^{-5}$ (emu/mol Oe)	Adj. R^2
100–300	2	−48.5(1)	0.80(1)	7.30(1)	0.9959(6)
150–300	2	−35.9(1)	0.75(1)	8.92(1)	0.9946(7)
100–300	5	−44.5(1)	0.77(1)	5.30(1)	0.9996(5)
150–300	5	−40.2(1)	0.80(1)	3.72(1)	0.9993(6)
100–300	10	−40.3(1)	0.74(1)	4.99(1)	0.9998(6)
150–300	10	−37.6(1)	0.78(1)	3.67(1)	0.9995(8)
100–300	30	−45.4(1)	0.73(1)	4.15(1)	0.9997(8)
150–300	30	−34.9(1)	0.73(1)	4.10(1)	0.9993(6)

Debye and three Einstein (1D + 3E) functions, yielding a Debye temperature of $\Theta_D \approx 100$ K and Einstein temperatures of $\Theta_{E1} \approx 654$ K, $\Theta_{E2} \approx 200$ K, and $\Theta_{E3} \approx 454$ K. During this fitting, C_D and C_{E_i} were assigned as weighting factors corresponding to the acoustic and optical modes of atomic vibrations, respectively, where $C_D : C_{E1} : C_{E2} : C_{E3} = 13.44 : 3.65 : 2.75 : 1.00$, resulting in the sum $C_D + \sum_i C_{E_i}$ equal to 20.64, which is close to the total number of atoms (20) per formula unit in $\text{Ba}_4\text{NbRh}_3\text{O}_{12}$. This fit was then extrapolated down to the lowest measured temperature [see Fig. 9(a)] and taken as the C_L , which was then subtracted from the total C_p . The estimated magnetic contribution to the specific heat (C_m) due to correlated Rh moments is shown in Fig. 9(b). It is possible that the lattice contribution to the specific heat is overestimated due to the relatively high energy scale of

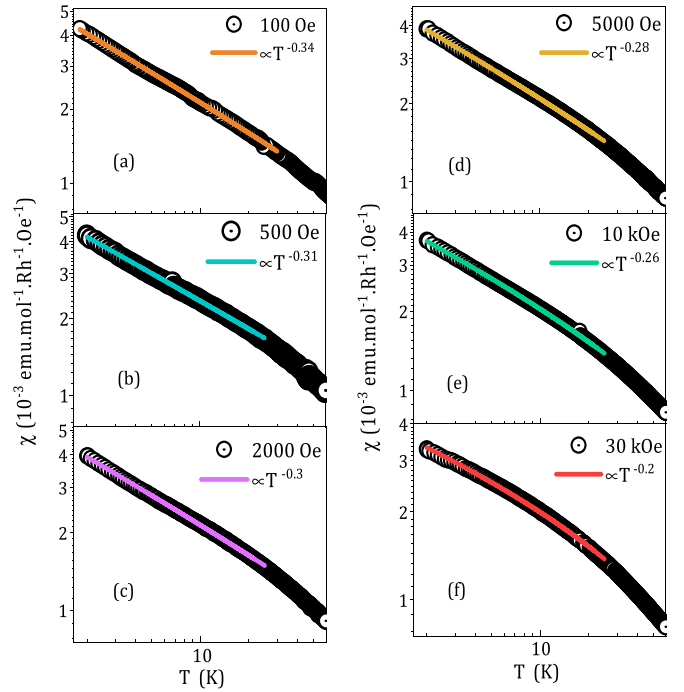


FIG. 12. [(a)–(f)] Temperature dependence of the dc magnetic susceptibility at different applied magnetic fields on a log-log scale, along with power-law fits (solid colored lines) in the 2 to 25 K range.

the intratrimer Rh-Rh direct exchange, compared to that of the 3d transition-metal ions, leading to an underestimate of the magnetic contribution to the total specific heat at higher temperatures.

- [1] Z. Zi-Hao and S. Lei, Muon spin relaxation studies on quantum spin liquid candidates, *Prog. Phys.* **40**, 143 (2020).
- [2] P. W. Anderson, The resonating valence bond state in La_2CuO_4 and superconductivity, *Science* **235**, 1196 (1987).
- [3] G. Baskaran, Z. Zou, and P. W. Anderson, The resonating valence bond state and high- T_c superconductivity – A mean field theory, *Solid State Commun.* **63**, 973 (1987).
- [4] L. Savary and L. Balents, Quantum spin liquids: a review, *Rep. Prog. Phys.* **80**, 016502 (2017).
- [5] L. Balents, Spin liquids in frustrated magnets, *Nature (London)* **464**, 199 (2010).
- [6] L. Clark, G. Sala, D. D. Maharaj, M. B. Stone, K. S. Knight, M. T. F. Telling, X. Wang, X. Xu, J. Kim, Y. Li, S.-W. Cheong, and B. D. Gaulin, Two-dimensional spin liquid behaviour in the triangular-honeycomb antiferromagnet TbInO_3 , *Nat. Phys.* **15**, 262 (2019).
- [7] T. Dey, A. V. Mahajan, P. Khuntia, M. Baenitz, B. Koteswararao, and F. C. Chou, Spin-liquid behavior in $J_{\text{eff}}=1/2$ triangular lattice compound $\text{Ba}_3\text{IrTi}_2\text{O}_9$, *Phys. Rev. B* **86**, 140405(R) (2012).
- [8] J. A. Quilliam, F. Bert, E. Kermarrec, C. Payen, C. Guillot-Deudon, P. Bonville, C. Baines, H. Luetkens, and P. Mendels, Singlet ground state of the quantum antiferromagnet $\text{Ba}_3\text{CuSb}_2\text{O}_9$, *Phys. Rev. Lett.* **109**, 117203 (2012).
- [9] K. Kitagawa, T. Takayama, Y. Matsumoto, A. Kato, R. Takano, Y. Kishimoto, S. Bette, R. Dinnebier, G. Jackeli, and H. Takagi, A spin-orbital-entangled quantum liquid on a honeycomb lattice, *Nature (London)* **554**, 341 (2018).
- [10] P. W. Anderson, Resonating valence bonds: A new kind of insulator? *Mater. Res. Bull.* **8**, 153 (1973).
- [11] M. Hermanns, I. Kimchi, and J. Knolle, Physics of the Kitaev model: Fractionalization, dynamic correlations, and material connections, *Annu. Rev. Condens. Matter Phys.* **9**, 17 (2018).
- [12] A. Kitaev, Anyons in an exactly solved model and beyond, *Ann. Phys. (NY)* **321**, 2 (2006).
- [13] S. H. Chun, J. W. Kim, J. Kim, H. Zheng, C. C. Stoumpos, C. D. Malliakas, J. F. Mitchell, K. Mehlawat, Y. Singh, Y. Choi, T. Gog, A. Al-Zein, M. M. Sala, M. Krisch, J. Chaloupka, G. Jackeli, G. Khaliullin, and B. J. Kim, Direct evidence for dominant bond-directional interactions in a honeycomb lattice iridate Na_2IrO_3 , *Nat. Phys.* **11**, 462 (2015).
- [14] L. S. I. Veiga, M. Etter, E. Cappelli, H. Jacobsen, J. G. Vale, C. D. Dashwood, D. Le, F. Baumberger, D. F. McMorrow, and R. S. Perry, Correlated electron metal properties of the honeycomb ruthenate Na_2RuO_3 , *Phys. Rev. Mater.* **4**, 094202 (2020).
- [15] V. V. Gapontsev, E. Z. Kurmaev, C. I. Sathish, S. Yun, J.-G. Park, and S. V. Streltsov, Spectral and magnetic properties of Na_2RuO_3 , *J. Phys.: Condens. Matter* **29**, 405804 (2017).

- [16] L. T. Nguyen and R. J. Cava, Hexagonal perovskites as quantum materials, *Chem. Rev.* **121**, 2935 (2021).
- [17] A. Nag, S. Middey, S. Bhowal, S. K. Panda, R. Mathieu, J. C. Orain, F. Bert, P. Mendels, P. G. Freeman, M. Mansson, H. M. Ronnow, M. Telling, P. K. Biswas, D. Sheptyakov, S. D. Kaushik, V. Siruguri, C. Meneghini, D. D. Sarma, I. Dasgupta, and S. Ray, Origin of the spin-orbital liquid state in a nearly $J=0$ iridate $\text{Ba}_3\text{ZnIr}_2\text{O}_9$, *Phys. Rev. Lett.* **116**, 097205 (2016).
- [18] A. Nag, S. Bhowal, F. Bert, A. D. Hillier, M. Itoh, I. Carlomagno, C. Meneghini, T. Sarkar, R. Mathieu, I. Dasgupta, and S. Ray, $\text{Ba}_3\text{M}\text{Ir}_2\text{O}_9$ hexagonal perovskites in the light of spin-orbit coupling and local structural distortions, *Phys. Rev. B* **97**, 064408 (2018).
- [19] Md S. Khan, A. Bandyopadhyay, A. Nag, V. Kumar, A. V. Mahajan, and S. Ray, Magnetic ground state of the distorted $6H$ perovskite $\text{Ba}_3\text{CdIr}_2\text{O}_9$, *Phys. Rev. B* **100**, 064423 (2019).
- [20] J. Chakraborty, Interplay of covalency, spin-orbit coupling, and geometric frustration in the $d^{3.5}$ system $\text{Ba}_3\text{LiIr}_2\text{O}_9$, *Phys. Rev. B* **97**, 235147 (2018).
- [21] T. Dey, R. Kumar, A. V. Mahajan, S. D. Kaushik, and V. Siruguri, Unconventional magnetism in the spin-orbit-driven Mott insulators $\text{Ba}_3\text{M}\text{Ir}_2\text{O}_9$ ($M=\text{Sc}, \text{Y}$), *Phys. Rev. B* **89**, 205101 (2014).
- [22] T. Dey, M. Majumder, J. C. Orain, A. Senyshyn, M. Prinz-Zwick, S. Bachus, Y. Tokiwa, F. Bert, P. Khuntia, N. Büttgen, A. A. Tsirlin, and P. Gegenwart, Persistent low-temperature spin dynamics in the mixed-valence iridate $\text{Ba}_3\text{InIr}_2\text{O}_9$, *Phys. Rev. B* **96**, 174411 (2017).
- [23] R. Kumar, D. Sheptyakov, P. Khuntia, K. Rolfs, P. G. Freeman, H. M. Ronnow, T. Dey, M. Baenitz, and A. V. Mahajan, $\text{Ba}_3\text{M}_x\text{Ti}_{3-x}\text{O}_9$ ($M = \text{Ir}, \text{Rh}$): A family of $5d/4d$ -based diluted quantum spin liquids, *Phys. Rev. B* **94**, 174410 (2016).
- [24] I. Terasaki, T. Igarashi, T. Nagai, K. Tanabe, H. Taniguchi *et al.*, Absence of magnetic long range order in $\text{Ba}_3\text{ZnRu}_2\text{O}_9$: A spin-liquid candidate in the $S = 3/2$ dimer lattice, *J. Phys. Soc. Jpn.* **86**, 033702 (2017).
- [25] J. Darriet, J. L. Soubeyroux, and A. P. Murani, Neutron inelastic scattering study of exchange interactions in a ruthenium V dimer $\text{Ba}_3\text{CaRu}_2\text{O}_9$, *J. Phys. Chem. Solids* **44**, 269 (1983).
- [26] Y. Shimoda, Y. Doi, M. Wakeshima, and Y. Hinatsu, Synthesis and magnetic properties of $12L$ -perovskites $\text{Ba}_4\text{LnIr}_3\text{O}_{12}$ ($\text{Ln} = \text{lanthanides}$), *J. Solid State Chem.* **182**, 2873 (2009).
- [27] Y. Shimoda, Y. Doi, M. Wakeshima, and Y. Hinatsu, Magnetic properties of quadruple perovskites $\text{Ba}_4\text{LnRu}_3\text{O}_{12}$ ($\text{Ln} = \text{La}, \text{Nd}, \text{Sm-Gd}, \text{Dy-Lu}$), *J. Solid State Chem.* **183**, 33 (2010).
- [28] L. T. Nguyen, T. Halloran, Weiwei Xie, T. Kong, C. L. Broholm, and R. J. Cava, Geometrically frustrated trimer-based Mott insulator, *Phys. Rev. Mater.* **2**, 054414 (2018).
- [29] L. T. Nguyen and R. J. Cava, Trimer-based spin liquid candidate $\text{Ba}_4\text{NbIr}_3\text{O}_{12}$, *Phys. Rev. Mater.* **3**, 014412 (2019).
- [30] J. Rodríguez-Carvajal, Recent advances in magnetic structure determination by neutron powder diffraction, *Phys. B: Condens. Matter* **192**, 55 (1993).
- [31] D. Takegami, L. Nicolai, T. C. Koethe, D. Kasinathan, C. Y. Kuo, Y. F. Liao, K. D. Tsuei, G. Panaccione, F. Offi, G. Monaco, N. B. Brookes, J. Minár, and L. H. Tjeng, Valence band hard x-ray photoelectron spectroscopy on $3d$ transition-metal oxides containing rare-earth elements, *Phys. Rev. B* **99**, 165101 (2019).
- [32] K. Koepf and H. Eschrig, Full-potential nonorthogonal local-orbital minimum-basis band-structure scheme, *Phys. Rev. B* **59**, 1743 (1999).
- [33] O. Arnold, J. C. Bilheux, J. M. Borreguero, A. Buts, S. I. Campbell, L. Chapon, M. Doucet, N. Draper, R. Ferraz Leal, M. A. Gigg *et al.*, Mantid-data analysis and visualization package for neutron scattering and μSR experiments, *Nucl. Instrum. Methods Phys. Res., Sect. A* **764**, 156 (2014).
- [34] F. M. F. de Groot, Z. W. Hu, M. F. Lopez, G. Kaindl, F. Guillot, and M. Tronc, Differences between L_3 and L_2 x-ray absorption spectra of transition metal compounds, *J. Chem. Phys.* **101**, 6570 (1994).
- [35] T. Burnus, Z. Hu, H. Wu, J. C. Cezar, S. Niitaka, H. Takagi, C. F. Chang, N. B. Brookes, H.-J. Lin, L. Y. Jang, A. Tanaka, K. S. Liang, C. T. Chen, and L. H. Tjeng, X-ray absorption and x-ray magnetic dichroism study on $\text{Ca}_3\text{CoRhO}_6$ and $\text{Ca}_3\text{FeRhO}_6$, *Phys. Rev. B* **77**, 205111 (2008).
- [36] J.-M. Chen, Y.-Y. Chin, M. Valldor, Z. Hu, J.-M. Lee, S.-C. Haw, N. Hiraoka, H. Ishii, C.-W. Pao, K.-D. Tsuei, J.-F. Lee, H.-J. Lin, L.-Y. Jang, A. Tanaka, C.-T. Chen, and L. H. Tjeng, A complete high-to-low spin state transition of trivalent cobalt ion in octahedral symmetry in $\text{SrCo}_{0.5}\text{Ru}_{0.5}\text{O}_{3-\delta}$, *J. Am. Chem. Soc.* **136**, 1514 (2014).
- [37] D. Takegami, D. Kasinathan, K. K. Wolff, S. G. Altendorf, C. F. Chang, K. Hofer, A. Melendez-Sans, Y. Utsumi, F. Meneghin, T. D. Ha, C. H. Yen, K. Chen, C. Y. Kuo, Y. F. Liao, K. D. Tsuei, R. Morrow, S. Wurmehl, B. Büchner, B. E. Prasad, M. Jansen *et al.*, Charge-transfer energy in iridates: A hard x-ray photoelectron spectroscopy study, *Phys. Rev. B* **102**, 045119 (2020).
- [38] A. Nag and S. Ray, Misjudging frustrations in spin liquids from oversimplified use of Curie-Weiss law, *J. Magn. Magn. Mater.* **424**, 93 (2017).
- [39] J. Terzic, J. C. Wang, F. Ye, W. H. Song, S. J. Yuan, S. Aswartham, L. E. DeLong, S. V. Streltsov, D. I. Khomskii, and G. Cao, Coexisting charge and magnetic orders in the dimer-chain iridate $\text{Ba}_5\text{Allr}_2\text{O}_{11}$, *Phys. Rev. B* **91**, 235147 (2015).
- [40] Y. S. Choi, C. H. Lee, S. Lee, S. Yoon, W.-J. Lee, J. Park, A. Ali, Y. Singh, J.-C. Orain, G. Kim, J.-S. Rhyee, W.-T. Chen, F. Chou, and K.-Y. Choi, Exotic low-energy excitations emergent in the random Kitaev magnet Cu_2IrO_3 , *Phys. Rev. Lett.* **122**, 167202 (2019).
- [41] C. Lee, S. Lee, Y. Choi, C. Wang, H. Luetkens, T. Shiroka, Z. Jang, Y.-G. Yoon, and K.-Y. Choi, Coexistence of random singlets and disordered Kitaev spin liquid in $\text{H}_3\text{LiIr}_2\text{O}_6$, *Phys. Rev. B* **107**, 014424 (2023).
- [42] I. Kimchi, J. P. Sheckelton, T. M. McQueen, and P. A. Lee, Scaling and data collapse from local moments in frustrated disordered quantum spin systems, *Nat. Commun.* **9**, 4367 (2018).
- [43] I. Kimchi, A. Nahum, and T. Senthil, Valence bonds in random quantum magnets: Theory and application to YbMgGaO_4 , *Phys. Rev. X* **8**, 031028 (2018).
- [44] J. Knolle, R. Moessner, and N. B. Perkins, Bond-disordered spin liquid and the honeycomb iridate $\text{H}_3\text{LiIr}_2\text{O}_6$: Abundant low-energy density of states from random Majorana hopping, *Phys. Rev. Lett.* **122**, 047202 (2019).
- [45] F. Bahrami, W. Lafargue-Dit-Hauret, O. I. Lebedev, R. Movshovich, H.-Y. Yang, D. Broido, X. Rocquefelte, and F. Tafti, Thermodynamic evidence of proximity to a Kitaev spin liquid in $\text{Ag}_3\text{LiIr}_2\text{O}_6$, *Phys. Rev. Lett.* **123**, 237203 (2019).

- [46] A. Bandyopadhyay, A. Chakraborty, S. Bhowal, V. Kumar, M. M. Sala, A. Efimenko, F. Bert, P. K. Biswas, C. Meneghini, N. Büttgen, I. Dasgupta, T. Saha Dasgupta, A. V. Mahajan, and S. Ray, Breakdown of atomic spin-orbit coupling picture in an apparently isolated pseudo-one-dimensional iridate: $\text{Sr}_3\text{NaIrO}_6$, *Phys. Rev. B* **105**, 104431 (2022).
- [47] Y. Li, D. Adroja, P. K. Biswas, P. J. Baker, Q. Zhang, J. Liu, A. A. Tsirlin, P. Gegenwart, and Q. Zhang, Muon spin relaxation evidence for the $U(1)$ quantum spin-liquid ground state in the triangular antiferromagnet YbMgGaO_4 , *Phys. Rev. Lett.* **117**, 097201 (2016).
- [48] S. Kundu, A. Shahee, A. Chakraborty, K. M. Ranjith, B. Koo, J. Sichelschmidt, M. T. F. Telling, P. K. Biswas, M. Baenitz, I. Dasgupta, S. Pujari, and A. V. Mahajan, Gapless quantum spin liquid in the triangular system $\text{Sr}_3\text{CuSb}_2\text{O}_9$, *Phys. Rev. Lett.* **125**, 267202 (2020).
- [49] S. Kundu, A. Hossain, P. Keerthi S., R. Das, M. Baenitz, P. J. Baker, J.-C. Orain, D. C. Joshi, R. Mathieu, P. Mahadevan, S. Pujari, S. Bhattacharjee, A. V. Mahajan, and D. D. Sarma, Signatures of a spin-1/2 cooperative paramagnet in the diluted triangular lattice of Y_2CuTiO_6 , *Phys. Rev. Lett.* **125**, 117206 (2020).
- [50] L. Clark, J. C. Orain, F. Bert, M. A. De Vries, F. H. Aidoudi, R. E. Morris, P. Lightfoot, J. S. Lord, M. T. F. Telling, P. Bonville, J. P. Attfield, P. Mendels, and A. Harrison, Gapless spin liquid ground state in the $S = 1/2$ vanadium oxyfluoride Kagome antiferromagnet $[\text{NH}_4]_2[\text{C}_7\text{H}_{14}\text{N}][\text{V}_7\text{O}_6\text{F}_{18}]$, *Phys. Rev. Lett.* **110**, 207208 (2013).
- [51] I. A. Campbell, A. Amato, F. N. Gygax, D. Herlach, A. Schenck, R. Cywinski, and S. H. Kilcoyne, Dynamics in canonical spin glasses observed by muon spin depolarization, *Phys. Rev. Lett.* **72**, 1291 (1994).
- [52] S. Kumar, S. K. Panda, M. M. Patidar, S. K. Ojha, P. Mandal, G. Das, J. W. Freeland, V. Ganesan, P. J. Baker, and S. Middey, Spin-liquid behavior of the three-dimensional magnetic system $\text{Ba}_3\text{NiIr}_2\text{O}_9$ with $S = 1$, *Phys. Rev. B* **103**, 184405 (2021).
- [53] C. Lacroix, P. Mendels, and F. Mila, *Introduction to Frustrated Magnetism: Materials, Experiments, Theory* (Springer Science & Business Media, New York, 2011), Vol. 164.
- [54] A. Yaouanc and P. Dalmas De Reotier, *Muon Spin Rotation, Relaxation, and Resonance: Applications to Condensed Matter* (Oxford University Press, Oxford, 2011).
- [55] J. G. Cheng, G. Li, L. Balicas, J. S. Zhou, J. B. Goodenough, C. Xu, and H. D. Zhou, High-pressure sequence of $\text{Ba}_3\text{NiSb}_2\text{O}_9$ structural phases: New $S = 1$ quantum spin liquids based on Ni^{2+} , *Phys. Rev. Lett.* **107**, 197204 (2011).
- [56] Y. Okamoto, M. Nohara, H. Aruga-Katori, and H. Takagi, Spin-liquid state in the $S = 1/2$ hyperkagome antiferromagnet $\text{Na}_4\text{Ir}_3\text{O}_8$, *Phys. Rev. Lett.* **99**, 137207 (2007).
- [57] Z. A. Kelly, M. J. Gallagher, and T. M. McQueen, Electron doping a kagome spin liquid, *Phys. Rev. X* **6**, 041007 (2016).
- [58] O. Mustonen, S. Vasala, E. Sadrollahi, K. P. Schmidt, C. Baines, H. C. Walker, I. Terasaki, F. J. Litterst, E. Baggio-Saitovitch, and M. Karppinen, Spin-liquid-like state in a spin-1/2 square-lattice antiferromagnet perovskite induced by $d^{10}-d^0$ cation mixing, *Nat. Commun.* **9**, 1085 (2018).
- [59] J. S. Helton, K. Matan, M. P. Shores, E. A. Nytko, B. M. Bartlett, Y. Yoshida, Y. Takano, A. Suslov, Y. Qiu, J.-H. Chung, D. G. Nocera, and Y. S. Lee, Spin dynamics of the spin-1/2 kagome lattice antiferromagnet $\text{ZnCu}_3(\text{OH})_6\text{Cl}_2$, *Phys. Rev. Lett.* **98**, 107204 (2007).
- [60] J. P. Shekellon, J. R. Neilson, D. G. Soltan, and T. M. McQueen, Possible valence-bond condensation in the frustrated cluster magnet $\text{LiZn}_2\text{Mo}_3\text{O}_8$, *Nat. Mater.* **11**, 493 (2012).
- [61] S. Yamashita, Y. Nakazawa, M. Oguni, Y. Oshima, H. Nojiri, Y. Shimizu, K. Miyagawa, and K. Kanoda, Thermodynamic properties of a spin-1/2 spin-liquid state in a κ -type organic salt, *Nat. Phys.* **4**, 459 (2008).
- [62] R. Tripathi, D. T. Adroja, C. Ritter, S. Sharma, C. Yang, A. D. Hillier, M. M. Koza, F. Demmel, A. Sundaresan, S. Langridge *et al.*, Quantum critical spin-liquid-like behavior in the $S = 1/2$ quasikagome-lattice compound $\text{CeRh}_{1-x}\text{Pd}_x\text{Sn}$ investigated using muon spin relaxation and neutron scattering, *Phys. Rev. B* **106**, 064436 (2022).
- [63] H. v. Löhneysen, A. Rosch, M. Vojta, and P. Wölfle, Fermi-liquid instabilities at magnetic quantum phase transitions, *Rev. Mod. Phys.* **79**, 1015 (2007).
- [64] Y. Li, H. Liao, Z. Zhang, S. Li, F. Jin, L. Ling, L. Zhang, Y. Zou, L. Pi, Z. Yang, J. Wang, Z. Wu, and Q. Zhang, Gapless quantum spin liquid ground state in the two-dimensional spin-1/2 triangular antiferromagnet YbMgGaO_4 , *Sci. Rep.* **5**, 16419 (2015).
- [65] A. Nag, S. Bhowal, A. Chakraborty, M. M. Sala, A. Efimenko, F. Bert, P. K. Biswas, A. D. Hillier, M. Itoh, S. D. Kaushik, V. Siruguri, C. Meneghini, I. Dasgupta, and S. Ray, Origin of magnetic moments and presence of spin-orbit singlets in Ba_2YIrO_6 , *Phys. Rev. B* **98**, 014431 (2018).
- [66] M. A. de Vries, A. C. McLaughlin, and J.-W. G. Bos, Valence bond glass on an fcc lattice in the double perovskite Ba_2YMoO_6 , *Phys. Rev. Lett.* **104**, 177202 (2010).
- [67] M. R. Norman and T. Micklitz, How to measure a spinon Fermi surface, *Phys. Rev. Lett.* **102**, 067204 (2009).
- [68] Y. Shen, Y.-D. Li, H. Wo, Y. Li, S. Shen, B. Pan, Q. Wang, H. C. Walker, P. Steffens, M. Boehm, Y. Hao, D. L. Quintero-Castro, L. W. Harriger, M. D. Frontzek, L. Hao, S. Meng, Q. Zhang, G. Chen, and J. Zhao, Evidence for a spinon Fermi surface in a triangular-lattice quantum-spin-liquid candidate, *Nature (London)* **540**, 559 (2016).
- [69] B. R. Ortiz, P. M. Sarte, A. H. Avidor, A. Hay, E. Kenney, A. I. Kolesnikov, D. M. Pajerowski, A. A. Aczel, K. M. Taddei, C. M. Brown, C. Wang, M. J. Graf, R. Seshadri, L. Balents, and S. D. Wilson, Quantum disordered ground state in the triangular-lattice magnet NaRuO_2 , *Nat. Phys.* **19**, 943 (2023).
- [70] J. M. Schliesser and B. F. Woodfield, Lattice vacancies responsible for the linear dependence of the low-temperature heat capacity of insulating materials, *Phys. Rev. B* **91**, 024109 (2015).
- [71] H. D. Zhou, E. S. Choi, G. Li, L. Balicas, C. R. Wiebe, Y. Qiu, J. R. D. Copley, and J. S. Gardner, Spin liquid state in the $S = 1/2$ triangular lattice $\text{Ba}_3\text{CuSb}_2\text{O}_9$, *Phys. Rev. Lett.* **106**, 147204 (2011).
- [72] S. Yamashita, T. Yamamoto, Y. Nakazawa, M. Tamura, and R. Kato, Gapless spin liquid of an organic triangular compound evidenced by thermodynamic measurements, *Nat. Commun.* **2**, 275 (2011).
- [73] T.-H. Han, R. Chisnell, C. J. Bonnoit, D. E. Freedman, V. S. Zapf, N. Harrison, D. G. Nocera, Y. Takano, and Y. S. Lee, Thermodynamic properties of the quantum spin liquid candidate $\text{ZnCu}_3(\text{OH})_6\text{Cl}_2$ in high magnetic fields, [arXiv:1402.2693v1](https://arxiv.org/abs/1402.2693v1).

- [74] S. Trebst, Kitaev materials, [arXiv:1701.07056](https://arxiv.org/abs/1701.07056).
- [75] M. J. Lawler, A. Paramakanti, Y. B. Kim, and L. Balents, Gapless spin liquids on the three-dimensional hyperkagome lattice of $\text{Na}_4\text{Ir}_3\text{O}_8$, *Phys. Rev. Lett.* **101**, 197202 (2008).
- [76] Y. Zhou, P. A. Lee, T.-K. Ng, and F.-C. Zhang, $\text{Na}_4\text{Ir}_3\text{O}_8$ as a 3D spin liquid with fermionic spinons, *Phys. Rev. Lett.* **101**, 197201 (2008).
- [77] P. Khuntia, S. Manni, F. R. Foronda, T. Lancaster, S. J. Blundell, P. Gegenwart, and M. Baenitz, Local magnetism and spin dynamics of the frustrated honeycomb rhodate Li_2RhO_3 , *Phys. Rev. B* **96**, 094432 (2017).
- [78] S. Xu, R. Bag, N. E. Sherman, L. Yadav, A. I. Kolesnikov, A. A. Podlesnyak, J. E. Moore, and S. Haravifard, Realization of U(1) Dirac quantum spin liquid in $\text{YbZn}_2\text{GaO}_5$, [arXiv:2305.20040](https://arxiv.org/abs/2305.20040).
- [79] S. Lee, D. Adroja, K. Y. Choi, and A. Berlie, μSR studies on the trimer-based quantum spin liquid candidates $\text{Ba}_4\text{NbM}_3\text{O}_{12}$, STFC ISIS Neutron and Muon Source, <https://doi.org/10.5286/ISIS.E.RB2010177> (2021).
- [80] S. D. A. Injac, Y. Xu, F. D. Romero, and Y. Shimakawa, Pauli-paramagnetic and metallic properties of high pressure polymorphs of BaRhO_3 oxides containing Rh_2O_9 dimers, *Dalton Trans.* **50**, 4673 (2021).